



## 저작자표시-비영리-변경금지 2.0 대한민국

이용자는 아래의 조건을 따르는 경우에 한하여 자유롭게

- 이 저작물을 복제, 배포, 전송, 전시, 공연 및 방송할 수 있습니다.

다음과 같은 조건을 따라야 합니다:



저작자표시. 귀하는 원저작자를 표시하여야 합니다.



비영리. 귀하는 이 저작물을 영리 목적으로 이용할 수 없습니다.



변경금지. 귀하는 이 저작물을 개작, 변형 또는 가공할 수 없습니다.

- 귀하는, 이 저작물의 재이용이나 배포의 경우, 이 저작물에 적용된 이용허락조건을 명확하게 나타내어야 합니다.
- 저작권자로부터 별도의 허가를 받으면 이러한 조건들은 적용되지 않습니다.

저작권법에 따른 이용자의 권리는 위의 내용에 의하여 영향을 받지 않습니다.

이것은 [이용허락규약\(Legal Code\)](#)을 이해하기 쉽게 요약한 것입니다.

[Disclaimer](#)

이학석사 학위논문

결정성 이산화티타늄 나노구조체의 제조,  
특성평가 및 광전적 응용에 관한 연구

**Fabrication, Characterization, and Photoelectric Application of  
Crystalline TiO<sub>2</sub> Nanostructures**

2014년 2월

서울대학교 대학원  
화학부 물리화학 전공  
이 대 기

**Fabrication, Characterization, and Photoelectric Application of  
Crystalline TiO<sub>2</sub> Nanostructures**

By Daeki Lee

Supervisor: Professor Du-Jeon Jang

Major: Physical Chemistry

School of Chemistry

Graduate School of Seoul National University

February 2014

결정성 이산화티타늄 나노구조체의 제조, 특성평가 및  
광전적 응용에 관한 연구

**Fabrication, Characterization, and Photoelectric Application of  
Crystalline TiO<sub>2</sub> Nanostructures**

지도교수 장 두 전

이 논문을 이학석사 학위논문으로 제출함  
2013년 10월

서울대학교 대학원  
화학부 물리화학 전공  
이 대 기

이대기의 이학석사 학위논문을 인준함  
2013년 12월

위 원 장	정 연 준 (서명)
부위원장	장 두 전 (서명)
위 원	강 현 (서명)

## **Abstract of Dissertation**

Crystalline TiO<sub>2</sub> nanostructures have been facilely grown on titanium foil via anodization and solvothermal processes and their morphological, structural, and optical properties have also been characterized. Photocatalytic and photovoltaic activities of TiO<sub>2</sub> nanostructures have been measured using the degradation of an organic dye under Xe-lamp irradiation.

Chapter 1 describes highly ordered and regularly porous anatase TiO<sub>2</sub> nanotube arrays grown by anodizing Ti foil in mixed viscous solvents of ethylene glycol and glycerol. By changing the volume ratio of two solvents, we have controlled the structural and morphological properties of TiO<sub>2</sub> nanotube arrays. Our prepared TiO<sub>2</sub> nanotube arrays have been found to have enhanced (004) planes, which are reactive in catalysis reactions. Among our prepared samples, TiO<sub>2</sub> nanotube arrays grown in 2:1 (v/v) ethylene glycol and glycerol have shown the best photocatalytic activity for the degradation of methylene blue and the highest photovoltaic conversion efficiency of 4.08%.

Chapter 2 reports anatase-rutile cocrystalline TiO<sub>2</sub> nanoblossoms fabricated via a one-step solvothermal process on Ti foil in mixed solvents of water and ethylene glycol. We have controlled the morphological, structural, and optical characteristics of TiO<sub>2</sub> nanoblossoms easily by changing the volume ratio of water and ethylene glycol. Cocrystalline structures of our prepared TiO<sub>2</sub> nanoblossoms act as nanoscale p-n junctions, which help to enhance the catalysis reactions. In particular, TiO<sub>2</sub> nanoblossoms grown in the 1:1 volume mixture of water and ethylene glycol show the best photocatalytic activity.

*Keywords:* TiO<sub>2</sub>, anodization, nanotube arrays, viscous solvents, solvothermal, nanoblossoms, nanoscale p-n junction, photoelectric

*Student Number:* 2011-23234

# **Contents**

<b>Abstract of Dissertation</b>	<b>i</b>
<b>List of Figures and Tables</b>	<b>1</b>
<b>Chapter 1. Facile Fabrication of Anatase TiO<sub>2</sub> Nanotube Arrays Having High Photocatalytic and Photovoltaic Performances by Anodization of Titanium in Mixed Viscous Solvents</b>	<b>5</b>
<b>1.1. Abstract</b>	<b>6</b>
<b>1.2. Introduction</b>	<b>7</b>
<b>1.3. Experimental Section</b>	<b>10</b>
<b>1.4. Results and discussion</b>	<b>13</b>
<b>1.5. Conclusions</b>	<b>24</b>
<b>1.6. Acknowledgments</b>	<b>25</b>
<b>1.7. Supporting Information</b>	<b>26</b>
<b>1.8. References</b>	<b>28</b>
<b>Chapter 2. Enhanced Photocatalytic Performances of Cocrystalline TiO<sub>2</sub> Nanoblossoms by the Effect of Nanoscale p-n Junctions</b>	<b>32</b>
<b>2.1. Abstract</b>	<b>33</b>
<b>2.2. Introduction</b>	<b>34</b>
<b>2.3. Experimental Section</b>	<b>37</b>

<b>2.4. Results and discussion</b>	<b>39</b>
<b>2.5. Conclusions</b>	<b>49</b>
<b>2.6. Acknowledgment</b>	<b>50</b>
<b>2.7. Supporting Information</b>	<b>51</b>
<b>2.8. References</b>	<b>53</b>
<b>Appendices</b>	<b>57</b>
<b>A.1. List of Presentations</b>	<b>57</b>
<b>Abstract (Korean)</b>	<b>58</b>



## List of Figures and Tables

**Figure 1-1.** FESEM side-view images of TiO<sub>2</sub> nanotube arrays grown on Ti foil in mixture electrolyte solutions of EG and glycerol with R values of (a) 0, (b) 0.5, (c) 1, and (d) 2. The insets, where each scale bar indicates 500 nm, show the FESEM top-view images of the corresponding TiO<sub>2</sub> nanotube arrays.

**Figure 1-2.** (a) TEM image, (b) HRTEM image, and (c) FFT pattern of a TiO<sub>2</sub> nanotube array grown on Ti foil in a 1:1 mixture solution of EG and glycerol.

**Figure 1-3.** HRXRD patterns of TiO<sub>2</sub> nanotube arrays grown on Ti foil in mixture electrolyte solutions of indicated R values. The standard diffraction lines of bare Ti foil and anatase TiO<sub>2</sub> are also shown for comparison.

**Figure 1-4.** Extinction spectra of the aqueous colloidal solutions of TiO<sub>2</sub> nanotube arrays grown on Ti foil in mixture electrolyte solutions of indicated R values. The right graphs indicate Kubelka-Munk plots after removal of scattering from the extinction spectra to find band-gap energies indicated in the units of eV.

**Figure 1-5.** Photoluminescence spectra of TiO<sub>2</sub> nanotube arrays grown on Ti foil in mixture electrolyte solutions of indicated R values. TiO<sub>2</sub> arrays were suspended in water and excited

at 266 nm.

**Figure 1-6.** (a) Photocatalytic absorption spectral changes of methylene blue(aq) in the presence of TiO<sub>2</sub> nanotube arrays grown at R = 1 with elapsed times indicated in the units of min. (b) First-order kinetic plots for the photocatalytic degradation of methylene blue in the presence of TiO<sub>2</sub> nanotube arrays grown at R values of (diamonds) 0, (closed triangles) 0.5, (circles) 1, and (squares) 2. The kinetic plot of crosses was obtained in the absence of TNAs while the plot of open triangles was measured in the absence of light with the presence of TNAs grown at R = 0.5. The rate constants obtained from the best-fitted lines are given in Table 1-1.

**Figure 1-7.** Current density-voltage characteristics of DSSCs wearing a light mask based on TiO<sub>2</sub> nanotube arrays grown on Ti foil in mixture electrolyte solutions of indicated R values.

**Table 1-1.** Mean crystallite diameters (d), band-gap energies (E<sub>g</sub>), maximum-PL wavelengths ( $\lambda_{\text{max}}$ ), and photodegradation catalysis rate constants (k) of TiO<sub>2</sub> nanotube arrays grown on Ti foil in mixture electrolyte solutions of EG and glycerol

**Table 1-2.** Photovoltaic operation parameters of DSSCs wearing a light mask produced with TiO<sub>2</sub> nanotube arrays grown on Ti foil in mixture electrolyte solutions of EG and glycerol

**Figure 2-1.** (a) TEM image and (b,c) HRTEM images of TiO<sub>2</sub> nanoblossoms grown on Ti foil in a mixture solvent of water and EG with  $f_w = 0.5$ . The HRTEM image and the FFT pattern of the panel b display the anatase structure while those of the panel c do the rutile structure.

**Figure 2-2.** FESEM images of TiO<sub>2</sub> nanoblossoms grown on Ti foil in mixture solvents of water and EG with  $f_w$  values of (a) 0.4, (b) 0.5, and (c) 0.6. Each scale bar indicates 1  $\mu\text{m}$ .

**Figure 2-3.** HRXRD patterns of TiO<sub>2</sub> nanoblossoms grown on Ti foil in mixture solvents of water and EG with indicated  $f_w$  values. The standard diffraction lines of anatase and rutile TiO<sub>2</sub> are also shown for comparison. The asterisks indicate diffraction peaks of bare Ti foil.

**Figure 2-4.** Absorption spectra of the aqueous colloidal solutions of TiO<sub>2</sub> nanoblossoms grown on Ti foil in mixture solvents of water and EG with indicated  $f_w$  values. The right graphs indicate Kubelka-Munk plots after removal of scattering from the extinction spectra to find the band gap energies indicated in the units of eV.

**Figure 2-5.** Photoluminescence spectra of TiO<sub>2</sub> nanoblossoms grown on Ti foil in mixture solvents of water and EG with indicated  $f_w$  values. TiO<sub>2</sub> nanoblossoms were suspended in water and excited at 266 nm.

**Figure 2-6.** Photocatalytic absorption spectral changes of methylene blue(aq) in the

presence of TiO<sub>2</sub> nanoblossoms grown at (a)  $f_w = 0.5$  and (b)  $f_w = 1$  with elapsed times indicated in the units of min. (c) First-order kinetic plots for the photocatalytic degradation of methylene blue in the presence of TiO<sub>2</sub> nanoblossoms grown at  $f_w$  values of (diamonds) 0.4, (triangles) 0.5, (circles) 0.6, and (squares) 1. The kinetic plot of crosses was obtained in the absence of TiO<sub>2</sub> nanoblossoms. The rate constants obtained from the best-fitted lines are given in Table 2-1.

**Table 2-1.** anatase fractions ( $f_{\text{anatase}}$ ), band-gap energies ( $E_g$ ), maximum-PL wavelengths ( $\lambda_{\text{max}}$ ), and photodegradation catalysis rate constants ( $k$ ) of TiO<sub>2</sub> nanoblossoms grown on Ti foil in mixture solvents of water and EG

**Chapter 1. Facile Fabrication of Anatase TiO<sub>2</sub> Nanotube Arrays Having High Photocatalytic and Photovoltaic Performances by Anodization of Titanium in Mixed Viscous Solvents**

## 1.1. Abstract

Highly ordered, vertically aligned, one side-opened, and regularly porous anatase  $\text{TiO}_2$  nanotube arrays have been facilely grown by anodizing Ti foil in mixed viscous solvents of ethylene glycol and glycerol. By changing the volume ratio of two solvents, we have controlled the structural properties of  $\text{TiO}_2$  nanotube arrays such as tube diameters, wall thicknesses, and tube lengths. Our prepared  $\text{TiO}_2$  nanotube arrays have been found to have enhanced (004) planes, which are reactive in catalysis reactions. We have demonstrated that  $\text{TiO}_2$  nanotube arrays grown in 2:1 (v/v) ethylene glycol and glycerol have the lowest band-gap energy and the largest mean crystallite diameter.  $\text{TiO}_2$  nanotube arrays grown on Ti foil have been directly employed for photocatalytic materials and the working electrode of photovoltaic dye-sensitized solar cells. Among our prepared samples,  $\text{TiO}_2$  nanotube arrays grown in 2:1 (v/v) ethylene glycol and glycerol have shown the best photocatalytic activity for the degradation of methylene blue and the highest photovoltaic conversion efficiency of 4.08%.

## 1.2. Introduction

The controlled fabrication, characterization, and application of nanometer-sized materials with functional properties have been studied extensively.<sup>1-4</sup> Particularly, semiconductor nanostructures have been intensively investigated to enhance their applications in diverse fields such as optoelectronics, transistors, and catalysts.<sup>5-9</sup> Among semiconductor materials, TiO<sub>2</sub> has been widely used in hydrogen generation, gas sensing, photocatalysis, dye-sensitized solar cells (DSSCs), and biomedical applications<sup>10-14</sup> because of its wide band-gap energy (3.2 eV for the anatase structure and 3.0 eV for the rutile structure). Furthermore, TiO<sub>2</sub> could be utilized as photocatalysts in aqueous conditions because its conduction-band position (-0.3 eV) is more negative than the reduction potential of hydrogen (0 eV). The waste water produced in textile and dye industry has a very bad effect on the environment due to their large discharge volume and toxic composition. With the development of dye industry, the treatment of waste water containing dyestuffs has become increasingly important.<sup>1</sup> The decomposition of these organic pollutants using photocatalysts is considered to be the most efficient green method for the management of organic pollutants. And, it has also been demonstrated that water can be electrochemically photolyzed into hydrogen and oxygen by using a semiconducting TiO<sub>2</sub> electrode.<sup>15</sup> Upon absorption of photons, a TiO<sub>2</sub> photocatalyst generates electron-hole pairs, called excitons, which are transferred to water subsequently. The transferred electrons initiate the reduction of protons to produce hydrogen while the transferred holes initiate the oxidation of water to produce oxygen. Generated excitons in the TiO<sub>2</sub> photocatalyst might also go through unwanted recombination. To prevent exciton recombination, the photocatalyst should have good crystallinity.<sup>16-20</sup> Other advantages of TiO<sub>2</sub> such as excellent electron mobility and good adsorption affinity toward organic molecules could allow TiO<sub>2</sub> to be used widely in applications.

Various fabrication methods of crystalline TiO<sub>2</sub> nanostructures have been reported in general: hydrothermal syntheses,<sup>21</sup> microwave-assisted hydrothermal syntheses,<sup>22</sup> chemical vapor deposition,<sup>23</sup> sol-gel reactions,<sup>17</sup> and electrochemical anodization processes. In particular, anodization processes<sup>24</sup> have attractive advantages for the fabrication of TiO<sub>2</sub> nanostructures; bare titanium is oxidized to produce titania with the form of nanotube arrays having pores of  $\leq 200$  nm in diameter. These tubular structures having large surface areas can be applied to membrane films; organic pollutants can be degraded through catalytic TiO<sub>2</sub> nanotubes. It is very innovative that the organic pollutants are self-purified over passing through a membrane catalyst with irradiation of light only.<sup>25</sup> In addition, the nanotube array structures function as channels through which electrons and holes generated by irradiated light can flow,<sup>26</sup> making electrons and holes transferred easily to target materials in contrast with aggregated nanoparticles. So, nanotube array structures receive special attention as electrodes of photovoltaic cells in electrochemical approaches. In anodization processes, the roles of electrolytes are very crucial because all the electrochemical reactions take place within electrolyte solutions. Macák *et al.*<sup>27</sup> have demonstrated that the morphologies of TiO<sub>2</sub> nanotube arrays depend on the type of electrolyte solutions; in glycerol-based electrolytes, TiO<sub>2</sub> nanotube arrays having smooth walls grow up whereas nanotube arrays with very rough and uneven walls grow up in aqueous electrolytes. In addition, Allam *et al.*<sup>28</sup> have reported that the crystallinity of TiO<sub>2</sub> nanotube arrays relies on the viscosity of the electrolyte solutions; the crystallinity of the TiO<sub>2</sub> nanotube arrays increases with the increasing viscosity of electrolytes. They have argued that ions have more time to migrate to crystalline lattice sites when the electrolytes are more viscous. So, it is expected that TiO<sub>2</sub> nanotube arrays grown up in an optimum electrolyte having an appropriate viscosity and a suitable molecular structure would show best catalytic performances. In electrochemical anodizing processes, polyols have been often employed as electrolyte solvents<sup>27-31</sup> because they could significantly



improve the regularity of anodized TiO<sub>2</sub> nanotube arrays.<sup>32</sup> In addition, polyols with multiple hydroxyl groups have a good solubility of water which is used as the oxygen source in the fabrication of TiO<sub>2</sub> nanotube arrays. Especially, ethylene glycol (EG) is widely used as an electrolyte solvent<sup>25,26,33-35</sup> owing to its low cost and easy approachableness. However, treatment to enhance the physical properties and the applicative performances of TiO<sub>2</sub> nanotube arrays via changing the composition of electrolyte solutions has not been reported yet, although this method could be a very simple and facile idea to improve the diverse properties of anodized TiO<sub>2</sub>.

In this work, anatase TiO<sub>2</sub> nanotube arrays have been fabricated through the electrochemical anodization of pure titanium foil in an NH<sub>4</sub>F-dissolved electrolyte solution containing EG and glycerol with a certain ratio. We have found an optimum electrolyte condition to make TiO<sub>2</sub> nanotube arrays with high photocatalytic and photovoltaic performances. Furthermore, we have controlled the structure, the length, and the pore diameter of TiO<sub>2</sub> nanotube arrays easily by changing the volume ratio of EG and glycerol. The crystallinity of fabricated anatase TiO<sub>2</sub> nanotube arrays has been found to be the highest in the electrolyte solution of 2:1 (v/v) EG and glycerol. TiO<sub>2</sub> nanotube arrays having the highest crystallinity have the best photocatalytic activity for the degradation of an organic dye under Xe-lamp irradiation and the highest photovoltaic power conversion efficiency of 4.08%.

### 1.3. Experimental Section

Ti foil(s, 0.25 mm thick,  $\geq 99.7\%$ ), Pt gauze(s, 100 mesh,  $\geq 99.9\%$ ),  $\text{NH}_4\text{F}$ (s,  $\geq 98\%$ ), methylene blue(s),  $\text{H}_2\text{PtCl}_6$ (s),  $\text{LiI}$ (s), 1-butyl-3-methylimidazolium iodide(l),  $\text{I}_2$ (s), guanidinium thiocyanate(l), acetonitrile(l), valeronitrile(l) and 4-*tert*-butylpyridine(l) were used as purchased from Sigma Aldrich. Ethylene glycol (EG, l,  $\geq 99\%$ ) and glycerol(l,  $\geq 99\%$ ) were purchased from Daejung Chemicals, N719 dye and Surlyn (SX1170-60) from Solaronix, and Pt-coated fluorine-doped tin oxide (FTO) glass ( $8\ \Omega\ \text{sq}^{-1}$ ) from Pilkington. Deionized water with a resistivity of  $\geq 18\ \text{M}\Omega\ \text{cm}$  from a Millipore Milli-Q system was used throughout the experiments.

Prior to anodization, Ti foil was rinsed sequentially with acetone, ethanol, and water. To grow  $\text{TiO}_2$  nanotube arrays, anodization has been performed for 2 h in a two-electrode system with Ti foil ( $1.5\ \text{cm} \times 1.5\ \text{cm}$ ) as the anode and Pt gauze ( $2.5\ \text{cm} \times 2.5\ \text{cm}$ ) as the cathode under 60 V using a DC power supply (E3612A, Agilent Technologies). All the electrochemical reactions were proceeded at  $25\ ^\circ\text{C}$  in a thermostatic water vessel. The electrolyte consisted of 0.17 M  $\text{NH}_4\text{F}$  and 2.0 vol%  $\text{H}_2\text{O}$  in EG and glycerol mixed at a certain volume ratio of glycerol to EG (R). As-anodized  $\text{TiO}_2$  nanotube arrays were washed in ethanol, dried via  $\text{N}_2$ (g) blowing, and annealed at  $500\ ^\circ\text{C}$  for 3 h with a temperature-rising rate of  $1\ ^\circ\text{C}\ \text{min}^{-1}$ .

The photocatalytic activities of our  $\text{TiO}_2$  nanotube arrays have been evaluated by monitoring the degradation of 1.2 ppm methylene blue in 10 mL water under light irradiation of a 300 W xenon lamp ( $290\ \text{mW}\ \text{cm}^{-2}$ ) with stirring continuously. Before being irradiated to Xe lamp light, each sample was stirred in the dark for 2 h to allow it to reach a complete adsorption-desorption equilibrium. To estimate the photovoltaic ability of our  $\text{TiO}_2$  nanotube

arrays, the energy-conversion efficiency of a DSSC with TiO<sub>2</sub> nanotube arrays was measured. For dye adsorption, the working electrode of TiO<sub>2</sub> nanotube arrays grown on Ti foil was immersed in anhydrous ethanol containing 0.5 mM N719 dye<sup>36</sup> and kept at room temperature for 24 h. The counter electrode was prepared by dropping 60  $\mu$ L of 0.5 mM H<sub>2</sub>PtCl<sub>6</sub>(aq) on an FTO glass followed by being heated at 400 °C for 20 min in air. Then, the working electrode of TiO<sub>2</sub> nanotube arrays on Ti foil and the counter electrode were placed to face each other and the mutual distance was controlled to be 60  $\mu$ m by using a Surlyn film. The transmittance of Pt-coated FTO was 72% at 500 nm. The electrolyte consisted of 0.1 M guanidinium thiocyanate, 0.5 M 4-*tert*-butylpyridine, 0.03 M I<sub>2</sub>, 0.02 M LiI, and 0.6 M 1-butyl-3-methylimidazolium iodide in 85:15 (v/v) acetonitrile and valeronitrile.<sup>37,38</sup> The device area of the dye-coated TiO<sub>2</sub> film was 0.220 cm<sup>2</sup>, and a light blocking mask was put on the device for accurate measurements.

Field emission-scanning electron microscope (FESEM) images were obtained with an FEI INSPECT F50 microscope, and transmission electron microscopy (TEM) and high-resolution TEM (HRTEM) images and fast Fourier transform (FFT) patterns with a JEOL JEM-3000F microscope. High-resolution X-ray diffraction (HRXRD) patterns were recorded using a Bruker D8 DISCOVER diffractometer with Cu K $\alpha$  radiation ( $\lambda$  = 0.154178 nm). Extinction spectra were measured by using a Scinco S-3100 UV/vis spectrometer, and emission spectra were obtained with a home-built fluorometer consisting of a Xe lamp of 75 W (Acton Research, XS432) with a monochromator of 0.15 m (Acton Research, Spectrapro-150) and a photomultiplier tube (Acton Research, PD438) attached to a monochromator of 0.30 m (Acton Research, Spectropro-300). Photocurrent-voltage (I-V) measurements were performed using a Keithley 2400 source measurement unit. A 300 W Xe lamp (Oriel Instruments, TLS-300X) was used as the light source to irradiate the counter electrode side of

the fabricated DSSC. The light intensity was adjusted using an NREL-calibrated Si solar cell equipped with a KG-5 filter to be AM 1.5G one sun light intensity approximately.

## 1.4. Results and discussion

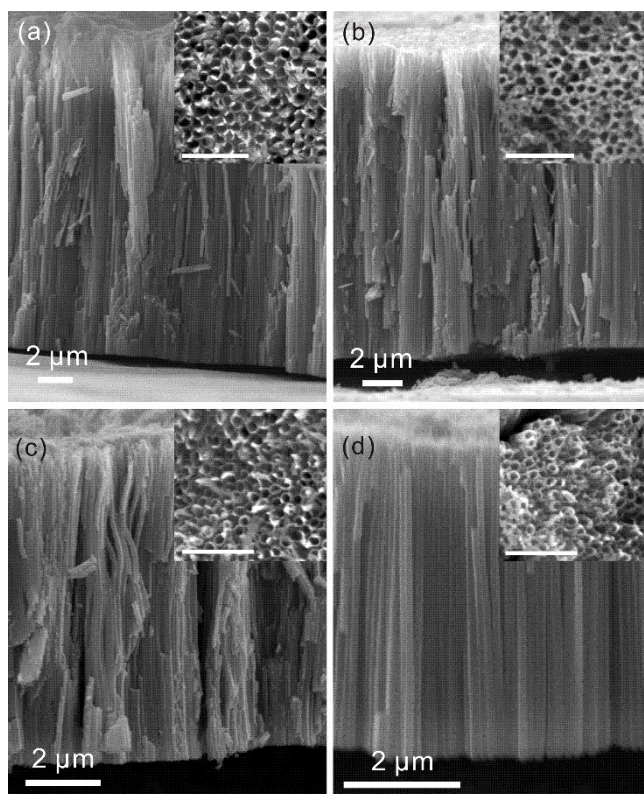


**Figure 1-1.** FESEM side-view images of TiO<sub>2</sub> nanotube arrays grown on Ti foil in mixture electrolyte solutions of EG and glycerol with R values of (a) 0, (b) 0.5, (c) 1, and (d) 2. The insets, where each scale bar indicates 500 nm, show the FESEM top-view images of the corresponding TiO<sub>2</sub> nanotube arrays.

Figure 1-1 shows that all the TiO<sub>2</sub> nanotube arrays (TNAs) grown on Ti foil in mixture electrolyte solutions of EG and glycerol have highly ordered, vertically aligned, one side-opened structures with uniform pores. Average inner diameters of TNAs were 61, 52, 44, and 37 nm and average wall thicknesses of TNAs were found to be 15, 15, 16, and 18 nm when R values were 0, 0.5, 1, and 2, respectively. Thus, we have demonstrated that anodized TNAs have smaller pores and thicker walls as they were grown at a higher value of R. In addition, the lengths of the TiO<sub>2</sub> nanotube arrays have showed a tendency to decrease with the increasing viscosity of the mixture electrolyte solution; the average lengths of the TiO<sub>2</sub>

nanotube arrays were 18, 15, 9, and 6  $\mu\text{m}$  when R values were 0, 0.5, 1, and 2, respectively. The observed characteristic properties of TNAs depending on R can be explained by the variation of the diffusion coefficient of the charge carrier that depends on the viscosity of the electrolyte solution. According to the Stokes-Einstein relation, the diffusion constant of a substance is inversely proportional to the viscosity of the solvent. Thus, the diffusion of a charge carrier becomes slow to decrease the current density of an electrochemical cell when the electrolyte solution is viscous.<sup>27</sup> The decrease of the current density could lead to the decrement of oxygen supply, decreasing the oxidation rate of Ti(s) and consequently slowing down the growth of TNAs.<sup>32</sup> The chemically dissolving rate of the produced titania is also slowed down<sup>32,39</sup> to produce TNAs with small pores and thick walls. The high-magnification side-view images of TNAs in Figure 1-S1 in the Supporting Information indicate that the surfaces of TNAs become smoother with the viscosity increase of the electrolyte solution. Irregular surfaces of TNAs can be explained by pH bursts at the pores of TNAs;<sup>27</sup> the chemical-dissolution rate of  $\text{TiO}_2$  is highly dependent on the pH value of the electrolyte solution,<sup>39</sup> and local acidification leads to a temporarily increased dissolution rate which generates an irregular wall surface. Thus, pH bursts at the pore tips of  $\text{TiO}_2$  nanotubes are correlated with the irregularity of the wall surfaces of TNAs, although pH bursts can be defused by increasing the viscosity of the electrolyte solution. Uniformly flat walls of TNAs are considered to be essential from the point of view of optical devices, where light transmission is severely reduced by diffuse scattering at morphological inhomogeneities.

The TEM image of Figure 1-2a suggests that our TNA has well-defined and highly ordered nanotubes as shown in Figure 1-1. The HRTEM image of Figure 1-2b and the FFT pattern of Figure 1-2c provide the microstructural details of our anatase TNA. The observed lattice-fringe distance of 0.235 nm in Figure 1-2b agrees reasonably with the spacing of 0.237

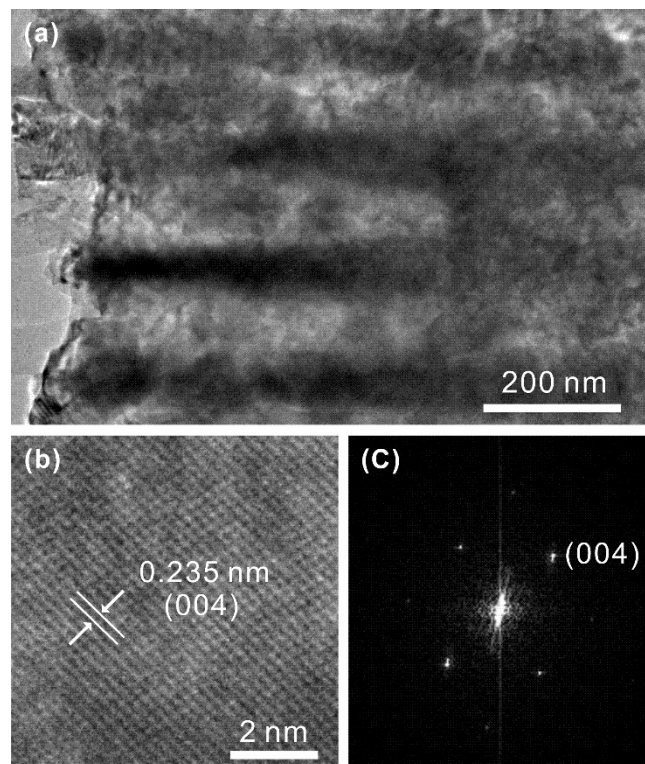


**Figure 1-2.** (a) TEM image, (b) HRTEM image, and (c) FFT pattern of a TiO<sub>2</sub> nanotube array grown on Ti foil in a 1:1 mixture solution of EG and glycerol.

nm between the (004) planes of the reference tetragonal anatase TiO<sub>2</sub> crystal (JCPDS card no. 84-1286). The average d-spacing value of 0.235 nm observed from the FFT pattern of Figure 1-2c also corresponds reasonably with the standard spacing of 0.237 nm between the (004) planes of the tetragonal anatase TiO<sub>2</sub>. The observed (004) planes of the anatase TiO<sub>2</sub> nanotube arrays in Figure 1-2b are dominant in the {001} facets. It has been reported that the order of the average surface energies is  $\gamma\{001\}$  (0.90 J m<sup>-2</sup>) >  $\gamma\{110\}$  (0.53 J m<sup>-2</sup>) >  $\gamma\{101\}$  (0.44 J m<sup>-2</sup>).<sup>40,41</sup> Although anatase TiO<sub>2</sub> nanoparticles exposing the {001} planes have hardly been observed due to the minimization of the surface energy during a crystal-growth process,<sup>6,42</sup> the TiO<sub>2</sub> nanotube of Figure 1-2b and c shows the (004) planes dominantly.

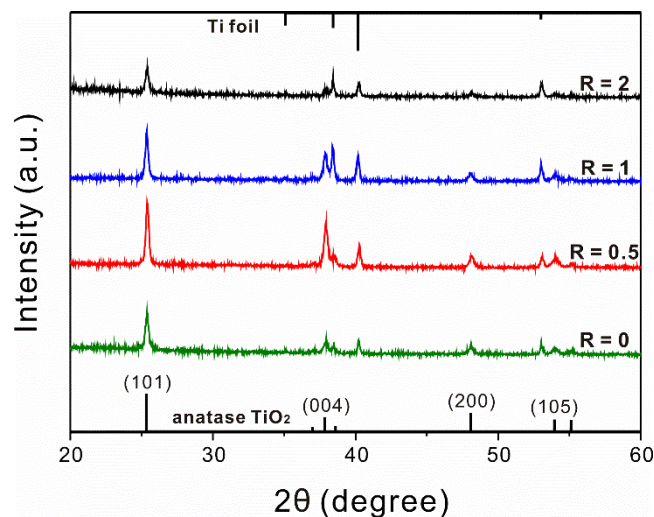


**Figure 1-3.** HRXRD patterns of  $\text{TiO}_2$  nanotube arrays grown on Ti foil in mixture electrolyte solutions of indicated R values. The standard diffraction lines of bare Ti foil and anatase  $\text{TiO}_2$  are also shown for comparison.

The HRXRD patterns in Figure 1-3 show that all our prepared  $\text{TiO}_2$  nanotube arrays have the tetragonal anatase  $\text{TiO}_2$  structure with lattice constants of  $a = b = 3.782 \text{ \AA}$  and  $c = 9.502 \text{ \AA}$  (JCPDS card no. 84-1286). All the HRXRD peaks of TNAs can be indexed to the standard peaks of the anatase  $\text{TiO}_2$  structure showing a strong preferential orientation of the (101) planes. Especially, the  $\text{TiO}_2$  nanotube arrays grown in a mixture electrolyte solution with  $R = 0.5$  have the best crystallinity of the anatase structure. The high viscosity of electrolyte solutions improves the crystalline quality of the resulting nanotube arrays by affecting the degree of oxide dissolution.<sup>43</sup> A low diffusion coefficient originated from the high viscosity of electrolyte solutions allows a chance for atoms to move to stable positions.<sup>29</sup> For this reason, the crystallinity of the anodized  $\text{TiO}_2$  nanotube arrays tends to increase with the viscosity increase of electrolyte solutions. It has been reported that the crystallinity of TNAs changes as a function of the viscosity of polyol electrolyte solutions; the intensity of the anatase (101) reflection increases with the viscosity increment of polyol electrolyte solutions.<sup>28</sup> When the viscosity of the electrolyte is too high, the mobility of charge carriers in the electrolyte is heavily slowed down, and it is rather hard for ions to find lattice sites. As a



result, TNAs grown with  $R = 2$  have a poor crystallinity of the anatase structure. We can extend this trend to the mean crystallite size of the anodized  $\text{TiO}_2$  nanotube arrays, which can be determined from the line width of a HRXRD peak by using the Scherrer's equation.<sup>44,45</sup> The mean crystallite diameters of TNAs grown with  $R = 0, 0.5, 1$ , and  $2$  have been estimated to be  $30, 33, 32$ , and  $20$  nm, respectively, by using the  $(101)$  peak at  $2\theta = 25.4^\circ$ , supporting that TNAs grown with  $R = 0.5$  have the best crystallinity. (Table 1-1) Furthermore, the  $(004)$  peak is most enhanced in the HRXRD pattern of TNAs grown with  $R = 0.5$ . For this reason, the  $(004)$  planes have been observed easily in the HRTEM image of Figure 1-2b and in the FFT pattern of Figure 1-2c. A high photocatalytic efficiency is expected for our  $\text{TiO}_2$  nanotube arrays having the  $\{001\}$  facets preferentially because the  $\{001\}$  facets having a higher surface energy are more reactive for the dissociative adsorption of reactant molecules than the  $\{101\}$  facets.<sup>21,40,41</sup> The viscosity of the electrolyte solutions has been considered to play a crucial role in the fabrication of  $\text{TiO}_2$  nanotube arrays under anodization processes.<sup>28-30</sup> When the viscosity of the electrolyte is increased, the electrochemical oxidation of Ti foil, as well as the chemical dissolution of the oxide layer, is further slowed down. This may provide sufficient time for ions to move to the crystalline lattice sites at the thermodynamically stable state. Surface atoms are not bonded to the maximum number of nearest neighbors, and the bonds of these unsatisfied surface atoms give rise to a surface energy.<sup>46</sup> Thus, the fact that the  $\{001\}$  facets have the highest surface energy means that the bond energy of Ti in the  $(001)$  planes is larger than that in any other planes, implying that the  $(001)$  lattice sites are thermodynamically most stable. Thus, an appropriate viscosity of the electrolyte solutions provides a chance for atoms to settle to the stable  $(001)$  lattice sites, increasing the proportion of the  $(001)$  planes observed in the HRXRD patterns of TNAs.

**Table 1-1.** Mean crystallite diameters (d), band-gap energies ( $E_g$ ), maximum-PL wavelengths ( $\lambda_{\max}$ ), and photodegradation catalysis rate constants (k) of TiO<sub>2</sub> nanotube arrays grown on Ti foil in mixture electrolyte solutions of EG and glycerol

R	d from HRXRD (nm)	$E_g$ (eV)	d from $E_g$ (nm)	$\lambda_{\max}$ (nm)	$k^a$ (h <sup>-1</sup> )
0	30	3.40 (365) <sup>b</sup>	24	347 (100) <sup>c</sup>	0.473
0.5	33	3.38 (367)	25	349 (68)	0.612
1	32	3.38 (367)	25	346 (79)	0.430
2	20	3.51 (353)	19	343 (98)	0.344

<sup>a</sup> The photodegradation rate constant in the absence of TiO<sub>2</sub> nanotube arrays is 0.078 h<sup>-1</sup> while the degradation catalysis rate constant with TiO<sub>2</sub> arrays grown at R = 0.5 in the absence of light is 0.007 h<sup>-1</sup>. <sup>b</sup> Band-gap energy in the units of nm. <sup>c</sup> Relative PL intensity.

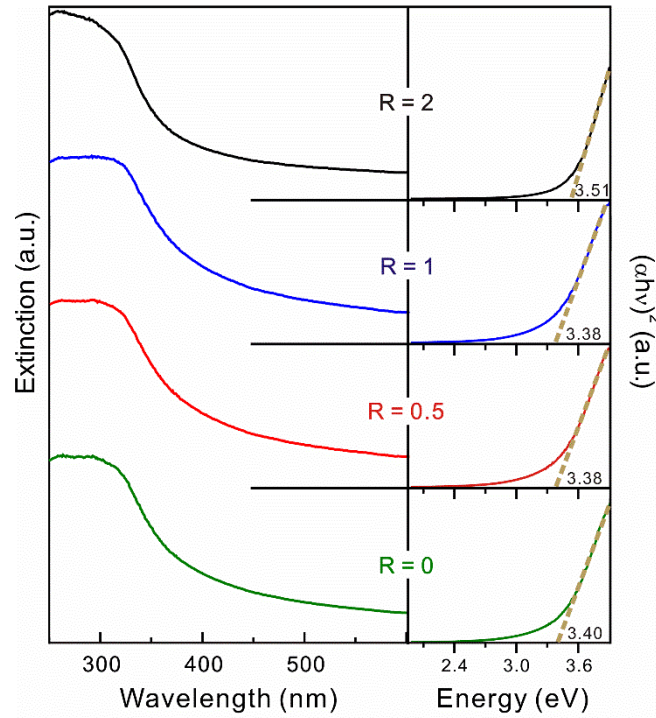


**Figure 1-4.** Extinction spectra of the aqueous colloidal solutions of TiO<sub>2</sub> nanotube arrays grown on Ti foil in mixture electrolyte solutions of indicated R values. The right graphs indicate Kubelka-Munk plots after removal of scattering from the extinction spectra to find band-gap energies indicated in the units of eV.

The extinction spectra in Figure 1-4 show that the absorption edges of all our prepared TNAs are shifted slightly to the blue, compared with those of typical bulk TiO<sub>2</sub> materials, due

to the quantum confinement effect. However, the extinction spectrum of TNAs grown with  $R = 0.5$  or  $1$  is less blue-shifted than that of TNAs grown with  $R = 0$  or  $2$ . This is attributed to the large crystallites of TNAs grown with  $R = 0.5$  and  $1$  as described with Figure 1-3. In the Kubelka-Munk plots of Figure 1-4, the intercepts of dashed lines correspond to the band-gap energies of as-prepared  $\text{TiO}_2$  nanotube arrays.<sup>47</sup> The band-gap energies of our TNAs have been found to be in the range of  $3.38 \sim 3.51$  eV. (Table 1-1) It has been reported that the band-gap energies of anatase  $\text{TiO}_2$  materials are about  $3.2$  eV for bulk and usually  $3.3$  eV for annealed crystalline TNAs.<sup>48</sup> The larger band-gap energies of our TNAs, than the conventional values of other  $\text{TiO}_2$  structures, could be attributed to the quantum size effect.<sup>29</sup> Coulombic interactions between electrons and holes cannot be neglected for nanoparticles. When the particle size decreases, the electron becomes closer to the hole to have a higher kinetic energy.<sup>49</sup> This may result in splitting of energy bands into discrete quantized levels and increasing of the band-gap energy.<sup>50</sup> Very tiny crystal grains of our TNAs with diameters of  $20 \sim 33$  nm could be expected to have the quantum size effect. Using the Brus equation<sup>51,52</sup> and the band-gap energies of TNAs obtained from Figure 1-4, average crystallite diameters of our TNAs grown with  $R = 0, 0.5, 1$ , and  $2$  have been calculated to be  $24, 25, 25$ , and  $19$  nm, respectively. The tendency is similar to that in the mean crystallite diameters of TNAs obtained from the HRXRD patterns of Figure 1-3.

The photoluminescence (PL) spectra of Figure 1-5 show that the dependence of the maximum-PL wavelengths of TNAs on  $R$  values is very similar to that of the band-gap energies of TNAs on  $R$  values. Especially, the PL spectrum of TNAs grown with  $R = 0.5$  is more red-shifted than any other TNAs (Table 1-1), also supporting that TNAs grown with  $R = 0.5$  have the best crystallinity. The PL spectrum of the anatase  $\text{TiO}_2$  can be considered to have three kinds of physical origins:<sup>53</sup> self-trapped excitons, oxygen vacancies, and surface

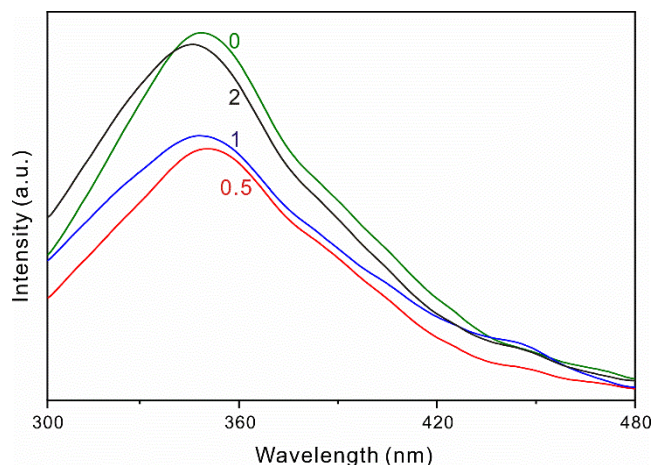


**Figure 1-5.** Photoluminescence spectra of TiO<sub>2</sub> nanotube arrays grown on Ti foil in mixture electrolyte solutions of indicated R values. TiO<sub>2</sub> arrays were suspended in water and excited at 266 nm.

states. Figure 1-5 and Table 1-1 indicate that the TNAs grown with  $R = 0.5$  have weaker PL than any other TNAs. This also suggests that our TNAs grown with  $R = 0.5$  have the best-defined -Ti-O- network of the anatase TiO<sub>2</sub> with a minimal amount of trap sites and oxygen vacancies, and demonstrates that our TNAs grown with  $R = 0.5$  have the best crystallinity of the anatase structure, consequentially.

The photocatalytic absorption spectral changes of the aqueous solution of methylene blue with time in Figure 1-6a show that the methylene blue dye was effectively degraded by the photocatalysis of our TNAs. When photons were absorbed into the TNA photocatalyst, generated holes were transferred to hydroxyl ions or water molecules to form hydroxyl radicals subsequently. These generated hydroxyl radicals could oxidize methylene blue to form Azure B, Azure A, Azure C, and thionine, etc., successively.<sup>54</sup> Thus, the absorbance of methylene blue was fallen down as time went on. Linear relationships in Figure 1-6b demonstrate that the photocatalytic degradation of methylene blue goes after the first-order kinetics of  $\ln(C/C_0) = -kt$ .<sup>55-57</sup> The first-order kinetic plots of Figure 1-6b indicate that the TiO<sub>2</sub> nanotube arrays grown with  $R = 0.5$  have the most efficient photocatalytic activity. The photodegradation rate constant in the presence of TNAs grown at  $R = 0.5$  is  $0.612 \text{ h}^{-1}$ ,

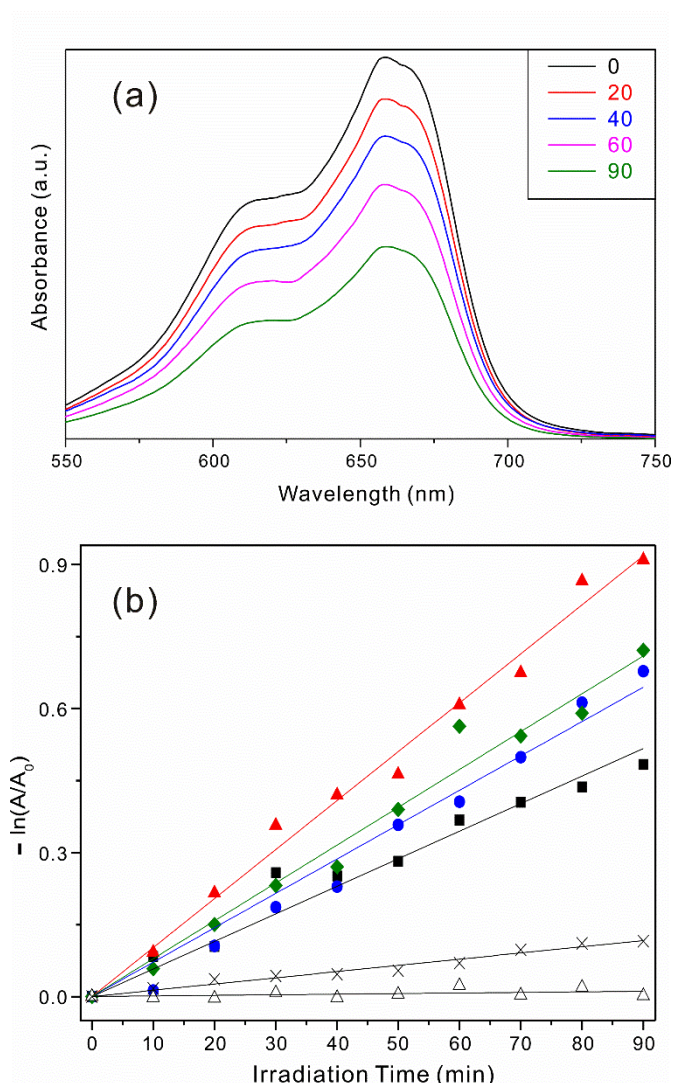


**Figure 1-6.** (a) Photocatalytic absorption spectral changes of methylene blue(aq) in the presence of TiO<sub>2</sub> nanotube arrays grown at R = 1 with elapsed times indicated in the units of min. (b) First-order kinetic plots for the photocatalytic degradation of methylene blue in the presence of TiO<sub>2</sub> nanotube arrays grown at R values of (diamonds) 0, (closed triangles) 0.5, (circles) 1, and (squares) 2. The kinetic plot of crosses was obtained in the absence of TNAs while the plot of open triangles was measured in the absence of light with the presence of TNAs grown at R = 0.5. The rate constants obtained from the best-fitted lines are given in Table 1-1.

whereas that in the absence of any TNAs is  $0.078 \text{ h}^{-1}$ , revealing the actual photocatalytic rate constant of the TNAs grown with R = 0.5 becomes  $0.534 \text{ h}^{-1}$ . The enhanced photocatalytic activity of TiO<sub>2</sub> nanotube arrays grown at R = 0.5 can be attributed to their appropriate tube length, smooth wall surface, good crystallinity, and low band-gap energy. In particular, the

highest crystallinity of TNAs grown with  $R = 0.5$  having the high surface energy  $\{001\}$  facets preferentially is considered to result in efficient photocatalytic performances. The degradation rate constant of methylene blue in the absence of light with TNAs grown at  $R = 0.5$  has been found to be as small as  $0.007 \text{ h}^{-1}$ , indicating that light must be irradiated for TNAs to function as a nanocatalyst.

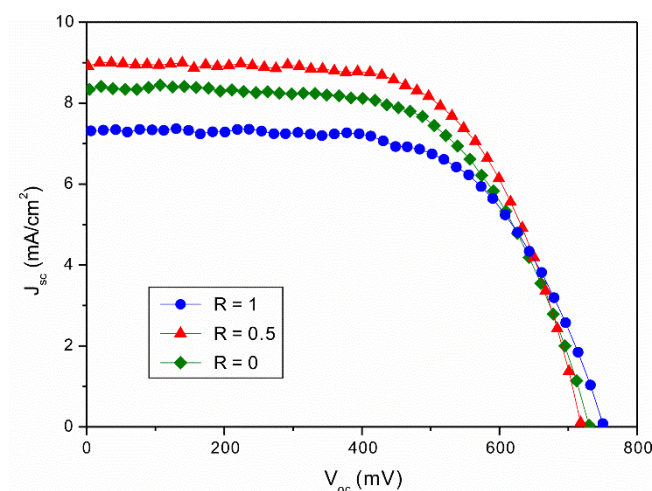


**Figure 1-7.** Current density-voltage characteristics of DSSCs wearing a light mask based on  $\text{TiO}_2$  nanotube arrays grown on Ti foil in mixture electrolyte solutions of indicated  $R$  values.

Figure 1-7 indicates the photovoltaic characters of the  $\text{TiO}_2$  nanotube arrays wearing a light mask while Figure 1-S2 and Table 1-S1 in the Supporting Information indicate those without a light mask, suggesting that our  $\text{TiO}_2$  nanotube arrays perform well as the working electrode of DSSC. The photovoltaic parameters of DSSCs obtained from the  $J$ - $V$  characteristic profiles of Figure 1-7 are listed in Table 1-2 to show that the open circuit voltages ( $V_{oc}$ ) have been found to be 731, 719, and 751 mV for DSSCs based on  $\text{TiO}_2$  nanotube arrays grown with  $R = 0, 0.5$ , and 1, respectively. However, the short-circuit current density ( $J_{sc}$ ) of  $8.927 \text{ mA cm}^{-2}$  from DSSC with TNAs grown at  $R = 0.5$  is higher than  $J_{sc}$

with any other TNAs. The highest current density can probably be attributed to the well-defined anatase crystallinity and the large surface area of TiO<sub>2</sub> nanotube arrays grown with R = 0.5 to absorb dye molecules most effectively.<sup>20,37,58-61</sup> In addition, because the nanotube array structures function as channels through which electrons and holes can move to the working and the counter electrodes of DSSC,<sup>26</sup> the best-defined anatase crystallinity of TNAs grown at R = 0.5 can enhance the mobility of electrons and holes to induce the highest current density. The low band-gap energy of TiO<sub>2</sub> nanotube arrays grown with R = 0.5 can also allow the enhanced absorption of irradiated light, leading to the enhanced photocurrent density. Table 1-2 summarizes that the TiO<sub>2</sub> nanotube arrays grown with R = 0.5 has the highest power conversion efficiency of 4.08%. Thus, we suggest that the highest power conversion efficiency using the TiO<sub>2</sub> nanotube arrays grown at R = 0.5 results from their large surface area to absorb dye molecules on a large scale, their well-defined anatase crystallinity to diminish electron-hole recombination, their highly ordered tubular structure to enhance the mobility of electrons and holes, and their low band-gap energy to absorb more photons.

**Table 1-2.** Photovoltaic operation parameters of DSSCs wearing a light mask produced with TiO<sub>2</sub> nanotube arrays grown on Ti foil in mixture electrolyte solutions of EG and glycerol

R	V <sub>oc</sub> (mV)	J <sub>sc</sub> (mA/cm <sup>2</sup> )	Fill Factor	Efficiency
0	730.6	8.353	61.69	3.76%
0.5	719.1	8.927	63.56	4.08%
1	751.3	7.322	62.87	3.46%

## 1.5. Conclusions

We have facilely fabricated highly ordered, vertically aligned, one side-opened, and regularly porous anatase  $\text{TiO}_2$  nanotube arrays (TNAs) by anodizing Ti foil in mixed viscous solvents of ethylene glycol (EG) and glycerol. The properties of  $\text{TiO}_2$  nanotube arrays have been controlled well by changing the viscosity of the mixed electrolyte solution.  $\text{TiO}_2$  nanotube arrays having the highest photocatalytic and photovoltaic performances have been fabricated at the optimum condition that the volume ratio of glycerol to EG (R) is 0.5.  $\text{TiO}_2$  nanotube arrays grown with  $R = 0.5$  have been found to have the highest crystallinity and the most enhanced (004) planes. Also, TNAs grown at  $R=0.5$  have the lowest band-gap energy, the largest mean crystallite diameters, and the best-defined  $-\text{Ti-O}-$  network of the anatase  $\text{TiO}_2$  structure with a minimal amount of trap sites and oxygen vacancies. The best photocatalytic activity of TNAs grown at  $R = 0.5$  is attributed to their appropriate tube length, smooth wall surface, well-ordered crystallinity, and low band-gap energy. The highest photovoltaic conversion efficiency of 4.08% with TNAs grown at  $R = 0.5$  as the working electrode of a dye-sensitized solar cell has also been attributed to their large surface, well-defined anatase crystallinity, highly ordered tubular structures, and low band-gap energy.



## **1.6. Acknowledgments**

This work was supported by the National Research Foundation of Korea (NRF) grant funded by the Korea government (MSIP) (No. 2011-0028981 and 2012-006345). D.J.J. is also thankful to the SRC program of NRF (2007-0056095).

## 1.7. Supporting Information

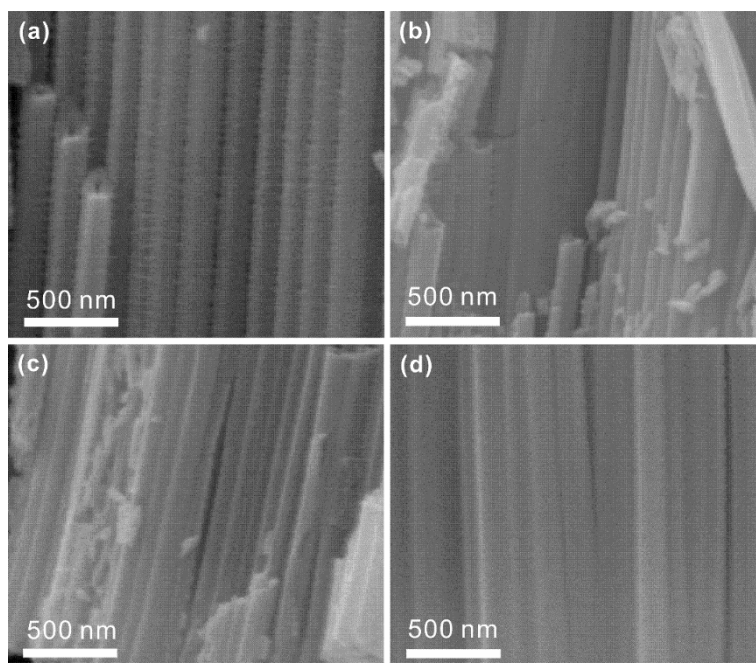


**Figure 1-S1.** FESEM side-view high magnification images of  $\text{TiO}_2$  nanotube arrays grown on Ti foil in mixture electrolyte solutions at R values of (a) 0, (b) 0.5, (c) 1, and (d) 2.

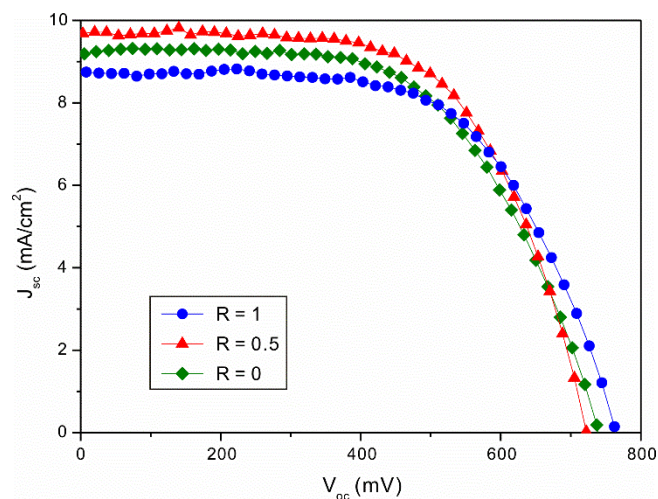


**Figure 1-S2.** Current density-voltage characteristics of DSSCs without a light mask based on  $\text{TiO}_2$  nanotube arrays grown on Ti foil in mixture electrolyte solutions of indicated R values.

**Table 1-S1.** Photovoltaic operation parameters of DSSCs without a light mask produced with TiO<sub>2</sub> nanotube arrays grown on Ti foil in mixture electrolyte solutions of EG and glycerol.

R	V <sub>oc</sub> (mV)	J <sub>sc</sub> (mA/cm <sup>2</sup> )	Fill Factor	Efficiency
0	739.5	9.217	59.52	4.06%
0.5	722.3	9.675	62.47	4.37%
1	764.1	8.748	61.41	4.10%

## 1.8. References

- [1] J.-A. Kwak, D. K. Lee and D.-J. Jang, *Appl. Catal. B: Environ.*, 2013, **142-143**, 323-328.
- [2] M. Son, S. J. Kim, J.-Y. Kim and D.-J. Jang, *J. Nanosci. Nanotech.*, 2013, **13**, 5777-5782.
- [3] S. E. Skrabalak, L. Au, X. Li and Y. Xia, *Nat. Protoc.*, 2007, **9**, 2182-2190.
- [4] M. R. Kim, J.-Y. Kim, S. J. Kim and D.-J. Jang, *Appl. Catal. A-Gen.*, 2011, **393**, 317-322.
- [5] Y.-Y. Zhang, J.-Y. Kim, Y. Kim and D.-J. Jang, *J. Nanopart. Res.*, 2012, **14**, 1117-1125.
- [6] A. Fujisjima, X. T. Zhang and D. A. Tryk, *Surf. Sci. Rep.*, 2008, **63**, 515-582.
- [7] J.-Y. Kim, H. Jeong and D.-J. Jang, *J. Nanopart. Res.*, 2011, **13**, 6699-6706.
- [8] H.-B. Kim and D.-J. Jang, *CrystEngComm*, 2012, **14**, 6946-6951.
- [9] Y. Kim, J.-Y. Kim and D.-J. Jang, *J. Phys. Chem. C*, 2012, **116**, 10296-10302.
- [10] E. Y. Kim, J. H. Park and G. Y. Han, *J. Power Sources*, 2008, **184**, 284-287.
- [11] S. Joo, I. Muto and N. Hara, *J. Electrochem. Soc.*, 2010, **157**, J221-J226.
- [12] S. B. Rawal, S. Bera, D. Lee, D.-J. Jang and W. I. Lee, *Catal. Sci. Technol.*, 2013, **3**, 1822-1830.
- [13] C. K. Xu, P. H. Shin, L. L. Cao, J. M. Wu and D. Gao, *Chem. Mater.*, 2010, **22**, 143-148.
- [14] O. K. Varghese, M. Paulose, T. J. LaTempa and C. A. Grimes, *Nano Lett.*, 2010, **10**, 750-750.
- [15] K. Honda and A. Fujishima, *Nature*, 1972, **238**, 37-38.
- [16] Y. Kuwahara and H. Yamashita, *J. Mater. Chem.*, 2011, **21**, 2407-2416.
- [17] F. Bosc, A. Ayral, P.-A. Albouy and C. Guizard, *Chem. Mater.*, 2003, **15**, 2463-2468.
- [18] J. J. Liao, S. W. Lin, L. Zhang, N. Q. Pan, X. K. Cao and J. B. Li, *ACS Appl. Mater. Interfaces*, 2012, **4**, 171-177.

- [19] W. Zhou, F. F. Sun, K. Pan, G. H. Tian, B. J. Jiang, Z. Y. Ren, C. G. Tian and H. G. Fu, *Adv. Funct. Mater.*, 2011, **21**, 1922-1930.
- [20] N. K. Allam, K. Shankar and C. A. Grimes, *Adv. Mater.*, 2008, **20**, 3942-3946.
- [21] J.-Y. Kim, D. Lee, H. J. Kim, I. Lim, W. I. Lee and D.-J. Jang, *J. Mater. Chem. A*, 2013, **1**, 5982-5988.
- [22] P. Periyat, N. Leyland, D. E. McCormack, J. Colreavy, D. Corr and S. C. Pillai, *J. Mater. Chem.*, 2010, **20**, 3650-3655.
- [23] J. W. Hou, X. C. Yang, X. Y. Lv, M. Huang, Q. Y. Wang and J. Wang, *J. Alloys Compd.*, 2012, **511**, 202-208.
- [24] V. Zwillling, M. Aucouturier and E. Darque-Ceretti, *Electrochim. Acta*, 1999, **45**, 921-929.
- [25] L.-L. Li, C.-Y. Tsai, H.-P. Wu, C.-C. Chen and E. W.-G. Diau, *J. Mater. Chem.*, 2010, **20**, 2753-2758.
- [26] J. Wang and Z. Lin, *Chem. Mater.*, 2008, **20**, 1257-1261.
- [27] J. M. Macak, H. Tsuchiya, L. Taveira, S. Aldabergerova and P. Schmuki, *Angew. Chem, Int., Ed.*, 2005, **44**, 7463-7465.
- [28] N. K. Allam and C. A. Grimes, *Langmuir*, 2009, **25**, 7234-7240.
- [29] J. Zhang, X. Tang and D. Li, *J. Phys. Chem. C*, 2011, **115**, 21529-21534.
- [30] S. Yoriya, G. K. Mor, S. Sharma and C. A. Grimes, *J. Mater. Chem.*, 2008, **18**, 3332-3336.
- [31] A. Mohammadpour, P. R. Waghmare, S. K. Mitra and K. Shankar, *ACS Nano*, 2010, **4**, 7421-7430.
- [32] Z. Su and W. Zhou, *J. Mater. Chem.*, 2011, **21**, 8955-8970.
- [33] G. Wang, H. Wang, Y. Ling, Y. Tang, X. Yang, R. C. Fitzmorris, C. Wang, J. Z. Zhang and Y.

Li, *Nano Lett.*, 2011, **11**, 3026-3033.

[34] M. Yang, H. Jha, N. Liu and P. Schmuki, *J. Mater. Chem.*, 2011, **21**, 15205-15208.

[35] G. Ali, S. H. Yoo, J. M. Kum, Y. N. Kim and S. O. Cho, *Nanotechnology*, 2011, **22**, 245602 (7pp).

[36] K. Shankar, G. K. Mor, H. E. Prakasam, S. Yoriya, M. Paulose, O. K. Varghese and C. A. Grimes, *Nanotechnology*, 2007, **18**, 065707 (11pp).

[37] S. H. Kang, S.-H. Choi, M.-S. Kang, J.-Y. Kim, H.-S. Kim, T. Hyeon and Y.-E. Sung, *Adv. Mater.*, 2008, **20**, 54-58.

[38] K.-S. Ahn, M.-S. Kang, J.-W. Lee and Y. S. Kang, *J. Appl. Phys.*, 2007, **101**, 084312 (5pages).

[39] J. M. Macak, H. Tsuchiya and P. Schmuki, *Angew. Chem, Int., Ed.*, 2005, **44**, 2100-2102.

[40] M. Liu, L. Y. Piao, L. Zhao, S. T. Ju, Z. J. Yan, T. He, C. L. Zhou, H. L. Li and W. J. Wang, *Chem. Commun.*, 2010, **46**, 1664-1666.

[41] U. Diebold, *Surf. Sci. Rep.*, 2003, **48**, 53-229.

[42] Y. Q. Dai, C. M. Cobley, J. Zeng, Y. M. Sun and Y. N. Xia, *Nano Lett.*, 2009, **9**, 2455-2459.

[43] N. R. de tacconi, C. R. Chenthamarakshan, G. Yogeeswaran, A. Watcharenwong, R. S. de Zoysa, N. A. Basit and K. Rajeshwar, *J. Phys. Chem. B*, 2006, **110**, 25347-25355.

[44] J.-Y. Kim, M. R. Kim, S.-Y. Park and D.-J. Jang, *CrystEngComm*, 2010, **12**, 1803-1808.

[45] R. J. Bandaranayake, G. W. Wen, L. Y. Lin, H. X. Jiang and C. M. Sorensen, *Appl. Phys. Lett.*, 1995, **67**, 831-833.

[46] W. D. Callister Jr., *Materials Science and Engineering: an Introduction*, John Wiley & Sons, New York, 6th edn., 2003, ch. 4, pp. 77-80.

[47] L. Li, Y.-W. Yang, G.-H. Li and L.-D. Zhang, *small*, 2006, **2**, 548-553.

- [48] A. M. Ferrari, D. Szieberth and Y. Noel, *J. Mater. Chem.*, 2011, **21**, 4568-4580.
- [49] T. Trindade, P. O'Brien and N. L. Pickett, *Chem. Mater.*, 2001, **13**, 3843-3858.
- [50] H. Weller, *Angew. Chem. Int. Ed.*, 1993, **32**, 41-53.
- [51] L. E. Brus, *J. Chem. Phys.*, 1984, **80**, 4403-4409.
- [52] K. M. Reddy, S. V. Manorama and A. R. Reddy, *Mater. Chem. Phys.*, 2003, **78**, 239-245.
- [53] Y. Lei, L. D. Zhang, G. W. Meng, G. H. Li, X. Y. Zhang, C. H. Liang, W. Chen and S. X. Wang, *Appl. Phys. Lett.*, 2001, **78**, 1125-1127.
- [54] J. Kim, W. Choi and H. Park, *Res. Chem. Intermed.*, 2010, **36**, 127-140.
- [55] T.-D. Nguyen-Phan and E. W. Shin, *J. Ind. Eng. Chem.*, 2011, **17**, 397-400.
- [56] F. X. Xiao, *J. Mater. Chem.*, 2012, **22**, 7819-7830.
- [57] P. Wilhelm and D. Stephan, *J. Photochem. Photobiol. A*, 2007, **185**, 19-25.
- [58] Z. H. Zhang and P. Wang, *Energy Environ. Sci.*, 2012, **5**, 6506-6512.
- [59] D. Zhao, T. Y. Peng, L. L. Lu, P. Cai, P. Jiang and Z. Q. Bian, *J. Phys. Chem. C*, 2008, **112**, 8486-8494.
- [60] J.-Y. Liao, B.-X. Lei, H.-Y. Chen, D.-B. Kuang and C.-Y. Su, *Energy Environ. Sci.*, 2012, **5**, 5750-5757.
- [61] N.-G. Park, J. van de Lagemaat and A. J. Frank, *J. Phys. Chem. B*, 2000, **104**, 8989-8994.

**Chapter 2. Enhanced Photocatalytic Performances of Cocrystalline TiO<sub>2</sub>  
Nanoblossoms by the Effect of Nanoscale p-n Junctions**



## 2.1. Abstract

Cocrystalline TiO<sub>2</sub> nanoblossoms having enhanced photocatalytic activities have been facilely grown via a one-step solvothermal process on titanium foil in mixed solvents of water and ethylene glycol. By varying the volume ratio of two solvents, we have controlled the morphological, the structural, and the optical properties of TiO<sub>2</sub> nanoblossoms. Our prepared TiO<sub>2</sub> nanoblossoms have been found to have both the anatase and the rutile crystal structures acting as nanoscale p-n junctions, which help to enhance catalytic performances via forming inner electric fields. In particular, TiO<sub>2</sub> nanoblossoms grown in the 1:1 volume mixture of water and ethylene glycol have been found to have the best-defined nanoscale p-n junctions, showing the best photocatalytic activity consequentially.

## 2.2. Introduction

The synthesis, characterization, and application of functional nanomaterials have been studied extensively.<sup>1-4</sup> Especially, the improvement of the chemical, electrical, and optical performances of semiconductor nanostructures has attracted a great attention in various applications such as catalysts, transistors, and optoelectronics.<sup>5-9</sup>  $\text{TiO}_2$  having a wide band-gap energy (3.2 eV for the anatase and 3.0 eV for the rutile) has been extensively used in biomedical applications, gas sensing, hydrogen generation, solar-energy conversion.<sup>10-14</sup>  $\text{TiO}_2$  has also been applied as photocatalysts to degrade organic pollutants with generation of hydroxyl radicals in aqueous conditions. The valence band position (2.9 eV) of  $\text{TiO}_2$ , which is more positive than the reduction potentials of a hydroxide ion (1.98 eV) and water (2.81 eV), can allow to generate hydroxyl radicals in the presence of light. When photons are absorbed into a  $\text{TiO}_2$  photocatalyst, generated holes are transferred to hydroxide ions or water to produce hydroxyl radicals subsequently. These generated hydroxyl radicals can oxidize organic pollutants consequently to produce useful oxide substances such as carbon dioxide, water, and acetone.<sup>15-19</sup> Untreated sewage produced in textile and dye industry adversely affects the environment due to their high toxicity and large discharge volume. With the development of industry, sewage disposal has become increasingly important.<sup>1</sup> The self-purification of organic pollutants using photocatalysts just requires irradiation of light, so it is considered to be the most efficient green method for the treatment of organic pollutants.

Crystalline  $\text{TiO}_2$  nanostructures have been synthesized via various approaches such as chemical vapor deposition,<sup>20</sup> electrochemical anodization processes,<sup>21</sup> microwave-assisted syntheses,<sup>22</sup> sol-gel reactions,<sup>23</sup> and hydrothermal and solvothermal syntheses<sup>24</sup>. In particular, solvothermal syntheses of  $\text{TiO}_2$  have attractive advantages such as environmental friendliness,

easy scale upwardness, and low production cost.<sup>25-27</sup> Especially, solvents can be changed variously for products to have desirous characteristic properties in solvothermal syntheses. Ethylene glycol (EG) has been most widely used as a solvent for syntheses of metal oxides because of its strong reducing capability, high boiling point, and high solubility of inorganic salts.<sup>28-34</sup> In addition, EG possessing two hydroxyl groups can dissolve water easily which is used as the oxygen source of metal oxides. EG is also used to control morphological properties of products; it has been reported that the use of EG as a solvent can induce nanostructures to form chain-like complexes with appropriate metal cations, which could readily aggregate into one-dimensional (1D) nanostructures within an isotropic medium.<sup>34</sup> Also, EG has relatively larger viscosity than other general solvents; the crystallinity of a TiO<sub>2</sub> nanomaterial has been reported to rely on the viscosity of a solvent.<sup>21</sup> So, it can be expected that TiO<sub>2</sub> nanostructures grown up in a viscous solvent like EG would show enhanced crystallinity and improved catalytic performances compared with formerly reported TiO<sub>2</sub> nanostructures.<sup>24</sup>

In this work, blossom-shaped TiO<sub>2</sub> nanoparticles having both the anatase and the rutile crystal structures, acting as nanoscale p-n junctions, have been facilely fabricated via a one-step solvothermal process using titanium foil in mixture solvents of water and EG at various ratios. Because as-synthesized TiO<sub>2</sub> nanoblossoms were grown on Ti foil, they could be directly and easily collected without employing any purification steps. We have controlled the morphological, structural, and optical characteristics of TiO<sub>2</sub> nanoblossoms easily by changing the volume ratio of water and EG. The proportion of the anatase structures in our TiO<sub>2</sub> nanoblossoms has been increased as the fraction of water in solvents increases. We have found that TiO<sub>2</sub> nanoblossoms grown in the 1:1 volume mixture of water and EG have well-defined nanoscale p-n junctions, which form inner electric fields to induce the best

photocatalytic activity for the degradation of an organic dye under Xe-lamp irradiation.

### 2.3. Experimental Section

Ti foil(s, 0.25 mm thick,  $\geq 99.7\%$ ),  $\text{H}_2\text{O}_2(\text{aq}, 30\%)$ ,  $\text{HF}(\text{aq}, 49\%)$ , and methylene blue(s) were used as purchased from Sigma Aldrich, while ethylene glycol (EG, 1,  $\geq 99\%$ ) was purchased from Daejung Chemicals. Deionized water with a resistivity of  $\geq 18 \text{ M}\Omega \text{ cm}$  from a Millipore Milli-Q system was used throughout the experiments.

Prior to the fabrication of  $\text{TiO}_2$  nanoblossoms, Ti foil was rinsed sequentially with acetone, ethanol, and water. 20  $\mu\text{L}$  of 30%  $\text{H}_2\text{O}_2(\text{aq})$ , 20  $\mu\text{L}$  of 49%  $\text{HF}(\text{aq})$ , and Ti foil ( $10 \times 20 \text{ mm}^2$ ) were added in mixed solvents of water and EG with a certain volume fraction of water ( $f_w = V_{\text{water}}/(V_{\text{water}} + V_{\text{EG}})$ ), and the resulting mixture was loaded into a Teflon-lined stainless-steel autoclave of 50 mL capacity. The autoclave was placed in an oven at 180  $^\circ\text{C}$  for 6 h and then cooled to room temperature. Prepared  $\text{TiO}_2$  nanoblossoms could be collected easily without employing any purification steps because they were grown on Ti foil without being dispersed in solvents. As-synthesized  $\text{TiO}_2$  nanoblossoms on Ti foil were washed with water to get rid of reactant residues and annealed at 500  $^\circ\text{C}$  for 3 h with a temperature-rising rate of 1  $^\circ\text{C min}^{-1}$ . The photocatalytic activities of our  $\text{TiO}_2$  nanoblossoms have been evaluated by monitoring the degradation of 7.2 ppm methylene blue in 2.0 mL of water under light irradiation of 290  $\text{mW cm}^{-2}$  from a 300 W Xe lamp with stirring continuously. Before being irradiated to Xe lamp light, each sample was stirred in the dark for 2 h to allow it to reach a complete adsorption-desorption equilibrium.

Transmission electron microscopy (TEM) and high-resolution TEM (HRTEM) images and fast Fourier transform (FFT) patterns were obtained with a JEOL JEM-3000F microscope, while field emission-scanning electron microscope (FESEM) images with a JEOL JSM-6700F microscope. High-resolution X-ray diffraction (HRXRD) patterns were recorded using

a Bruker D8 DISCOVER diffractometer with Cu K $\alpha$  radiation ( $\lambda = 0.154178$  nm). Absorption spectra were measured by using a Scinco S-3100 UV/vis spectrometer, and emission spectra were obtained with a home-built fluorometer consisting of a Xe lamp of 75 W (Acton Research, XS432) with a monochromator of 0.15 m (Acton Research, Spectrapro-150) and a photomultiplier tube (Acton Research, PD438) attached to a monochromator of 0.30 m (Acton Research, Spectropro-300).

## 2.4. Results and discussion

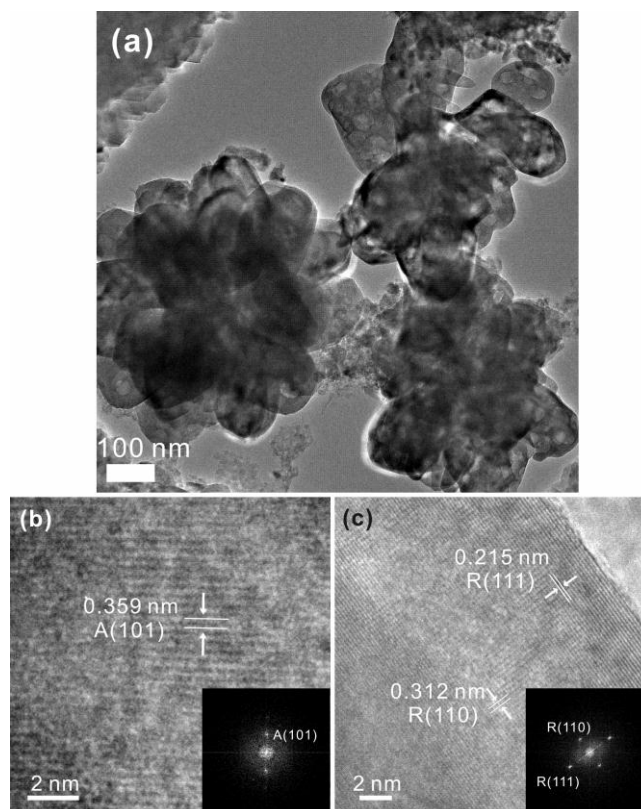


**Figure 2-1.** (a) TEM image and (b,c) HRTEM images of  $\text{TiO}_2$  nanoblossoms grown on Ti foil in a mixture solvent of water and EG with  $f_w = 0.5$ . The HRTEM image and the FFT pattern of the panel b display the anatase structure while those of the panel c do the rutile structure.

Figure 2-1a shows that  $\text{TiO}_2$  nanoparticles with blossom-like shapes have been grown directly on Ti foil in mixture solvents of water and EG; a lot of lumpy arms have been grown to form  $\text{TiO}_2$  nanoblossoms. The HRTEM image and the FFT pattern of Figure 2-1b provide the microstructural details of the anatase crystal structure in a  $\text{TiO}_2$  nanoblossom while Figure 2-1c shows the microstructural details of the rutile crystal structure. The observed lattice-fringe distance of 0.359 nm in Figure 2-1b agrees reasonably with the standard spacing of 0.351 nm between the (101) planes of the reference anatase  $\text{TiO}_2$  crystal (JCPDS card no. 84-1286), while 0.312 and 0.215 nm in Figure 2-1c correspond to 0.319 nm between the (110)

planes and 0.216 nm between the (111) planes of the reference rutile  $\text{TiO}_2$  crystal (JCPDS card no. 88-1175), respectively. And the average d-spacing value of 0.360 nm observed from the FFT pattern of the inset of Figure 2-1b also corresponds reasonably with the standard spacing of 0.351 nm between the (101) planes of the anatase  $\text{TiO}_2$ , while 0.320 and 0.210 nm observed from the FFT pattern of the inset of Figure 2-1c agree with the standard spacing of 0.319 nm between the (110) planes and that of 0.216 nm between the (111) planes of the rutile  $\text{TiO}_2$ , respectively. Thus, it is expected that our  $\text{TiO}_2$  nanoblossoms may have altered physical and catalytic properties resulting from the coexistence of these cocrystalline structures in a  $\text{TiO}_2$  nanoblossom. Figure 2-S1 in the Supporting Information shows that well-defined  $\text{TiO}_2$  nanoblossoms have also been grown at  $f_w$  values of 0.4 and 0.6. It have been found that the lumpy arms of  $\text{TiO}_2$  nanoblossoms become stumpy as the  $f_w$  value increases.

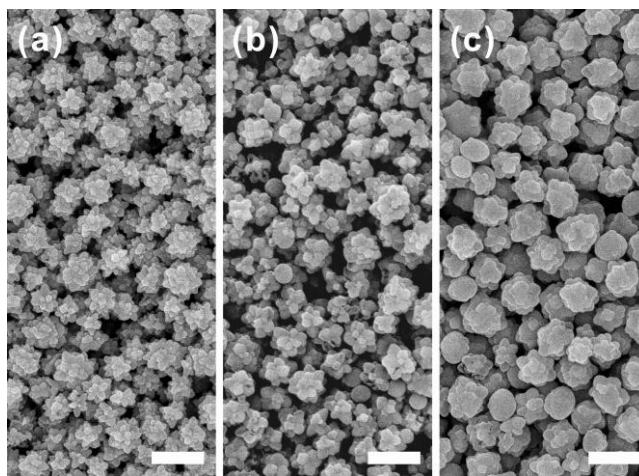
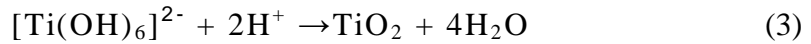
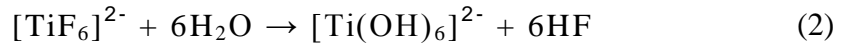


**Figure 2-2.** FESEM images of  $\text{TiO}_2$  nanoblossoms grown on Ti foil in mixture solvents of water and EG with  $f_w$  values of (a) 0.4, (b) 0.5, and (c) 0.6. Each scale bar indicates 1  $\mu\text{m}$ .

Figure 2-2 shows that the morphologies of  $\text{TiO}_2$  nanoblossoms grown on Ti foil in mixture solvents of water and EG have been changed with the variation of the fractional amount of water in solvents. The particle diameters of  $\text{TiO}_2$  nanoblossoms have been found to increase as the nanostructures were grown at a higher value of  $f_w$ ; the average diameters of



TiO<sub>2</sub> nanoblossoms were 490±80, 570±70, and 680±70 nm when  $f_w$  values were 0.4, 0.5, and 0.6, respectively. This observed tendency of TiO<sub>2</sub> nanoblossoms can be explained by considering the role of water in mixed solvents. When the  $f_w$  value increases, the amount of oxygen atoms supplied by water increases. Thus, the oxidation reaction of titanium is activated intensively and large sizes of TiO<sub>2</sub> nanoblossoms are achieved at a higher value of  $f_w$ . The oxidation and the hydrolysis of elemental titanium in solvents induce stepwise reactions to produce TiO<sub>2</sub> nanoblossoms as shown in eqs 1–3.<sup>35,36</sup>



In addition, FESEM images of Figure 2-2 show that the lumpy arms of TiO<sub>2</sub> nanoblossoms have become stumpy when the  $f_w$  value increases as described with TEM images of Figures 2-1 and S1. The average lengths of arms grown on TiO<sub>2</sub> nanoblossoms were 160±30, 140±30, and 130±40 nm when  $f_w$  values were 0.4, 0.5, and 0.6, respectively. Furthermore, the morphologies of TiO<sub>2</sub> nanoblossoms grown with low values of  $f_w$ , shown in Figure 2-S2 in the Supporting Information, suggest that the spiky arms of TiO<sub>2</sub> nanoblossoms have been swelled gradually to become lumpy as the  $f_w$  value increases. These observed morphological characteristics of TiO<sub>2</sub> nanoblossoms depending on  $f_w$  values can be explained by the effect of EG on metal oxides in mixture solvents. The use of EG as a solvent can induce nanostructures to form chain-like complexes with appropriate metal cations, which could readily aggregate into 1D nanostructures within an isotropic medium.<sup>34</sup> In the fabrication of titania, partially chelated titanium complexes are produced in the presence of EG as the glycolate ligand has a chelating feature.<sup>37</sup> Thus, EG serves not only as a solvent but

also as a bidentate chelate to bridge adjacent titanium atoms and to form 1D structures.<sup>29</sup> However, as the  $f_w$  value increases, the amount of EG is decreased while the amount of water is increased. This means that with the increase of  $f_w$ , the formation of 1D TiO<sub>2</sub> nanostructures becomes more difficult while the swelling of 1D TiO<sub>2</sub> nanostructures becomes easier. Thus, the spiky arms of TiO<sub>2</sub> nanostructures become lumpy and stumpy as the  $f_w$  value increases, and TiO<sub>2</sub> nanoblossoms can be fabricated on Ti foil in mixture solvents of water and EG with the  $f_w$  range of 0.4–0.6. Figure 2-S2a shows that no TiO<sub>2</sub> products were grown in water-free EG, indicating that EG could not serve as the oxygen source but that water only could supply oxygen atoms in the fabrication of TiO<sub>2</sub> nanoblossoms in our mixed solvents.

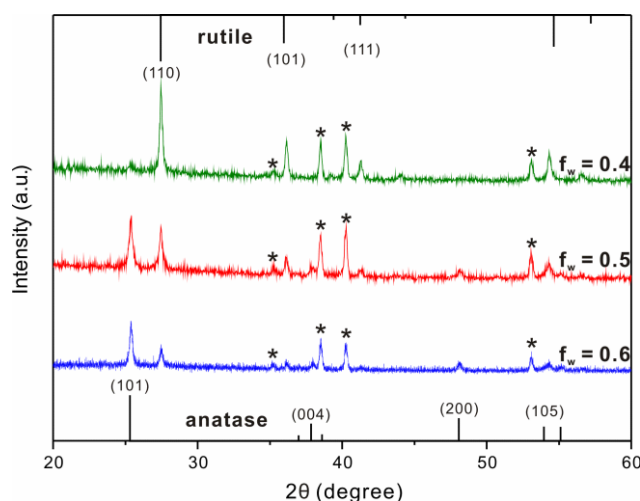


**Figure 2-3.** HRXRD patterns of TiO<sub>2</sub> nanoblossoms grown on Ti foil in mixture solvents of water and EG with indicated  $f_w$  values. The standard diffraction lines of anatase and rutile TiO<sub>2</sub> are also shown for comparison. The asterisks indicate diffraction peaks of bare Ti foil.

The HRXRD patterns in Figure 2-3 show that all our prepared TiO<sub>2</sub> nanoblossoms have crystallites of both the anatase (JCPDS card no. 84-1286) and the rutile (JCPDS card no. 88-1175) TiO<sub>2</sub> structures. For this reason, the microstructural details of both the anatase and the rutile crystal structures of our TiO<sub>2</sub> nanoblossoms have been observed in the HRTEM images and the FFT patterns of Figure 2-1. All the HRXRD peaks of TiO<sub>2</sub> nanoblossoms can be

indexed to the standard peaks of the anatase and the rutile  $\text{TiO}_2$  structures showing a strong preferential orientation of the anatase (101) or the rutile (110) planes. The fractions of the anatase structure obtained from  $I_{101(\text{anatase})}$  and  $I_{110(\text{rutile})}$  in Figure 2-3 are given in Table 2-1. It is found that the intensity of the rutile structure is decreased while the intensity of the anatase structure is enhanced as the  $f_w$  value increases. The properties of our mixed solvents have been considered to play a crucial role in the crystallite determination of  $\text{TiO}_2$  nanostructures. First,  $\text{H}_2\text{O}_2$  in solvents can react with  $\text{Ti}^{4+}$  ions to form a dinuclear complex,  $\text{Ti}_2\text{O}_5(\text{OH})_x^{(2-x)}$  ( $x = 1-6$ ),<sup>38,39</sup> which may retard the hydrolysis of the Ti precursor. The comparatively slow hydrolysis rate could provide enough time for the formation of Ti-O chains to grow crystalline crystals. Meanwhile, EG in mixture solvents can induce to produce partially chelated titanium complexes. The glycolate ligand has a chelating feature to prevent the approach of water molecules toward the central metal ion, slowing down significantly both the hydrolysis of  $[\text{TiF}_6]^{2-}$  and the subsequent condensation of  $[\text{Ti}(\text{OH})_6]^{2-}$ . Thus, EG in mixed solvents plays a key role to retard all the reactions of eqs 2 and 3.<sup>37</sup> In addition, it is reported that EG coordinates with metal ions first to form a complex as proved by the slow generation of the precipitate when reagents are mixed together; a relatively slow reaction rate is known to be crucial for the synthesis of high-quality crystals.<sup>33</sup> Also, EG has relatively larger viscosity than water. When the viscosity of a solvent is increased, the diffusion of ions in the solvent becomes to be slowed down. Eventually, the described retardation of reactions caused by EG may provide sufficient time for ions to move to the crystalline lattice sites of the thermodynamically stable state.<sup>21,40,41</sup> It is reported that the rutile  $\text{TiO}_2$  structure is fabricated at a higher crystallization temperature than the anatase structure,<sup>42,43</sup> implying that the rutile crystal structure is thermodynamically more stable than the anatase crystal structure. Thus, the retardation of reactions caused by EG provides a chance for atoms to settle down in the stable rutile lattice sites, increasing the proportion of the rutile peaks observed in the HRXRD

patterns of TiO<sub>2</sub> nanoblossoms. High photocatalytic efficiencies are expected in our TiO<sub>2</sub> nanoblossoms having cocrystalline structures because nanoscale p-n junctions exist at interfaces between the anatase and the rutile domains.<sup>40,44</sup> It has been reported<sup>45,46</sup> that the anatase and the rutile crystals act as n-type and p-type semiconductors, respectively. Near a p-n junction, electrons and holes diffuse to the p-n interface from the n-type and the p-type regions, respectively, inducing the formation of an inner electric field at the p-n interface. For photocatalytic materials, an inner electric field can help to enhance the photocatalytic efficiency.<sup>44</sup> Especially, TiO<sub>2</sub> nanoblossoms grown in a mixture solvent with  $f_w = 0.5$  have both the anatase and the rutile structures in an almost equal ratio, meaning that well-defined nanoscale p-n junctions are assembled successfully. The individual mean crystallite sizes of the anatase and the rutile crystal structures in TiO<sub>2</sub> nanoblossoms can be determined from the line widths of HRXRD peaks by using the Scherrer's equation.<sup>47,48</sup> The mean crystallite diameters of anatase crystals in TiO<sub>2</sub> nanoblossoms grown with  $f_w = 0.4, 0.5$ , and  $0.6$  have been estimated to be 18, 30, and 49 nm, respectively, by using the anatase (101) peak at  $2\theta = 25.3^\circ$ , while those of rutile crystals in TiO<sub>2</sub> nanoblossoms grown with  $f_w = 0.4, 0.5$ , and  $0.6$  have been measured to be 58, 36, and 24 nm, respectively, by using the rutile (110) peak at  $2\theta = 27.9^\circ$ , supporting that tiny domains consisting of the anatase and the rutile crystals of 33 nm in average diameter are dispersed well, and good nanoscale p-n junctions are formed consequently in TiO<sub>2</sub> nanoblossoms grown with  $f_w = 0.5$ . The HRXRD patterns of as-synthesized and annealed TiO<sub>2</sub> nanoblossoms grown with  $f_w = 0.5$  in Figure 2-S3 of the Supporting Information show that crystal structures of TiO<sub>2</sub> nanoblossoms have changed hardly via the annealing process, although the crystallinity of our TiO<sub>2</sub> nanoblossoms has been increased to a some degree. Incomplete crystallites detected at  $2\theta = 59^\circ$  have been disappeared clearly after annealing, supporting that the annealing process can improve the crystallinity of our TiO<sub>2</sub> nanoblossoms substantially.

**Table 2-1.** Anatase fractions ( $f_{\text{anatase}}$ ), band-gap energies ( $E_g$ ), maximum-PL wavelengths ( $\lambda_{\text{max}}$ ), and photodegradation catalysis rate constants ( $k$ ) of  $\text{TiO}_2$  nanoblossoms grown on Ti foil in mixture solvents of water and EG

$f_w$	$f_{\text{anatase}}^a$	$E_g^b$ (eV)	$\lambda_{\text{max}}$ (nm)	$k^c$ ( $\text{h}^{-1}$ )
0.4	0.10	2.92	391 (71) <sup>d</sup>	4.82
0.5	0.61	3.14	399 (100)	5.89
0.6	0.73	3.15	395 (92)	5.23

<sup>a</sup>  $I_{101(\text{anatase})} / (I_{101(\text{anatase})} + I_{110(\text{rutile})})$  in Figure 2-3. <sup>b</sup> The band-gap energy of  $\text{TiO}_2$  nanoblossoms grown at  $f_w = 1$  is 3.18 eV. <sup>c</sup> The photodegradation rate constant in the absence of  $\text{TiO}_2$  nanoblossoms is  $0.226 \text{ h}^{-1}$  while the photodegradation rate constant in the presence of  $\text{TiO}_2$  nanoblossoms grown at  $f_w = 1$  is  $3.63 \text{ h}^{-1}$ .

<sup>d</sup> Relative PL intensity.

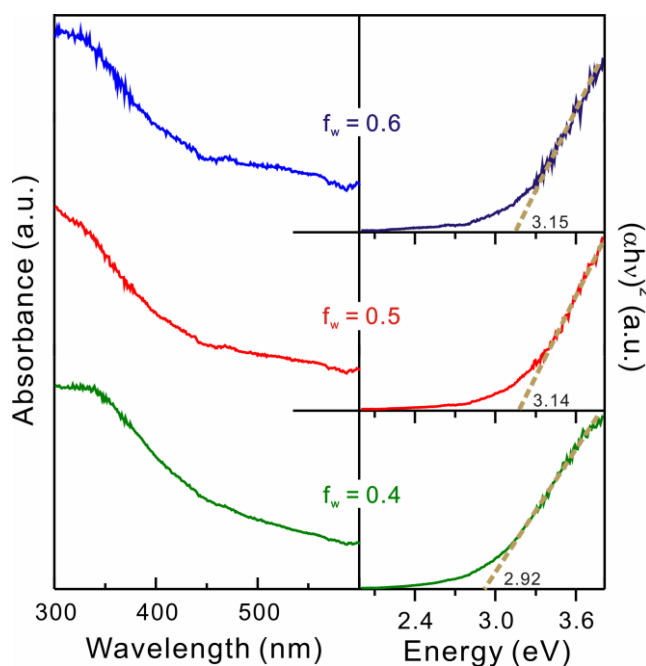


**Figure 2-4.** Absorption spectra of the aqueous colloidal solutions of  $\text{TiO}_2$  nanoblossoms grown on Ti foil in mixture solvents of water and EG with indicated  $f_w$  values. The right graphs indicate Kubelka-Munk plots to find the band-gap energies indicated in the units of eV.

The absorption spectra of Figure 2-4 show that the absorption edge of our prepared  $\text{TiO}_2$  nanoblossoms is shifted slightly to the blue as the  $f_w$  value is increased. This is attributed to

increase in the amount of anatase crystallites with the increase of the  $f_w$  value as described with Figure 2-3. It has been well known that the band-gap energy of the anatase  $\text{TiO}_2$  (3.2 eV) is larger than that of the rutile  $\text{TiO}_2$  (3.0 eV), supporting that the increase of anatase domains leads to the blue shift of the absorption edge of a  $\text{TiO}_2$  material. This trend is extended to the Kubelka-Munk plots that have been derived from the absorption spectra of our  $\text{TiO}_2$  nanoblossoms in Figure 2-4. In the Kubelka-Munk plots of Figure 2-4, the intercepts of dashed lines correspond to the band-gap energies of as-prepared  $\text{TiO}_2$  nanoblossoms.<sup>49</sup> The band-gap energies of our  $\text{TiO}_2$  nanoblossoms have been found to be in the range of 2.92–3.18 eV (Table 2-1), supporting that our  $\text{TiO}_2$  nanoblossoms lie within the band-gap range between the rutile and the anatase structures. Thus, we are suggesting that our  $\text{TiO}_2$  nanoblossoms consist of nanoscale anatase-rutile crystal junctions; the portion of anatase domains and the subsequent band-gap energy of  $\text{TiO}_2$  nanoblossoms increase with the increment of the  $f_w$  value.

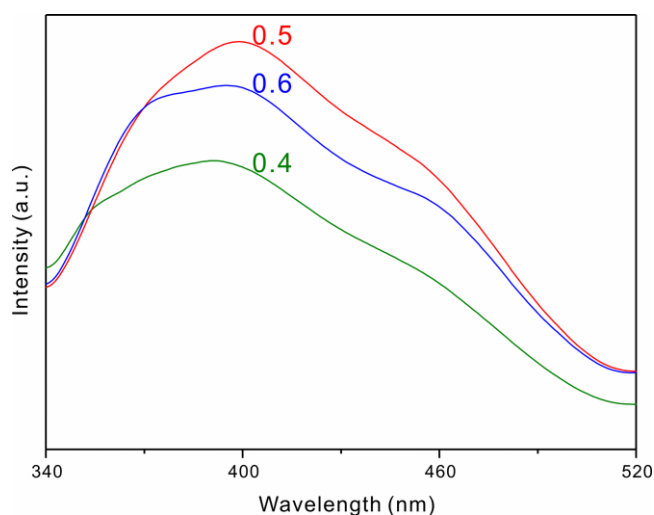


**Figure 2-5.** Photoluminescence spectra of  $\text{TiO}_2$  nanoblossoms grown on Ti foil in mixture solvents of water and EG with indicated  $f_w$  values.  $\text{TiO}_2$  nanoblossoms were suspended in water and excited at 266 nm.

The photoluminescence (PL) spectra of Figure 2-5 show that the spectrum of  $\text{TiO}_2$  nanoblossoms grown with  $f_w = 0.5$  is more red-shifted than any other  $\text{TiO}_2$  nanoblossoms.

(Table 2-1) The PL spectrum of a TiO<sub>2</sub> nanomaterial can be considered to have three kinds of physical origins:<sup>50</sup> self-trapped excitons, oxygen vacancies, and surface states. In this case, the PL spectrum of our TiO<sub>2</sub> nanoblossoms has been attributed mainly to oxygen vacancies because crystalline TiO<sub>2</sub> has an indirect band gap.<sup>51-54</sup> In particular, the long-wavelength side of the PL spectrum has been considered to result from oxygen vacancies. Thus, the fact that the PL spectrum of TiO<sub>2</sub> nanoblossoms grown at  $f_w = 0.5$  is most red-shifted in Figure 2-5 suggests that oxygen vacancies are most abundant in TiO<sub>2</sub> nanoblossoms grown at  $f_w = 0.5$ . Furthermore, Figure 2-5 and Table 2-1 indicate that TiO<sub>2</sub> nanoblossoms grown with  $f_w = 0.5$  have stronger PL than any other TiO<sub>2</sub> nanoblossoms, also suggesting that the amount of oxygen vacancies as well as trap sites is largest in our TiO<sub>2</sub> nanoblossoms grown with  $f_w = 0.5$ . These results support that incoherent lattice-lattice interfaces resulting from nanoscale anatase-rutile crystal junctions are richest in our TiO<sub>2</sub> nanoblossoms grown with  $f_w = 0.5$ ; the presence of vacancies or defects is inevitable near to nanoscale crystal junctions.

The photocatalytic absorption spectral changes of the aqueous solution of methylene blue with elapsed time in Figure 2-6a,b show that the organic dye of methylene blue was effectively degraded by the photocatalysis of our TiO<sub>2</sub> nanoblossoms. Especially, it is shown that the photocatalytic performances of TiO<sub>2</sub> nanoblossoms grown at  $f_w = 0.5$  (Figure 2-6a) are more efficient than those of TiO<sub>2</sub> nanoblossoms grown with  $f_w = 1$  (Figure 2-6b) at the same concentrations of photocatalysts. When light was irradiated to TiO<sub>2</sub> nanoblossoms, generated holes were transferred to hydroxyl ions or water molecules to produce hydroxyl radicals subsequently. These generated hydroxyl radicals could oxidize methylene blue to make the solution colorless gradually.<sup>55</sup> Thus, the absorbance of methylene blue declined with the elapsed time. Linear relationships in Figure 2-6c indicate that the photocatalytic degradation of methylene blue signifies the first-order kinetics of  $\ln(C/C_0) = -kt$ .<sup>56-58</sup> The

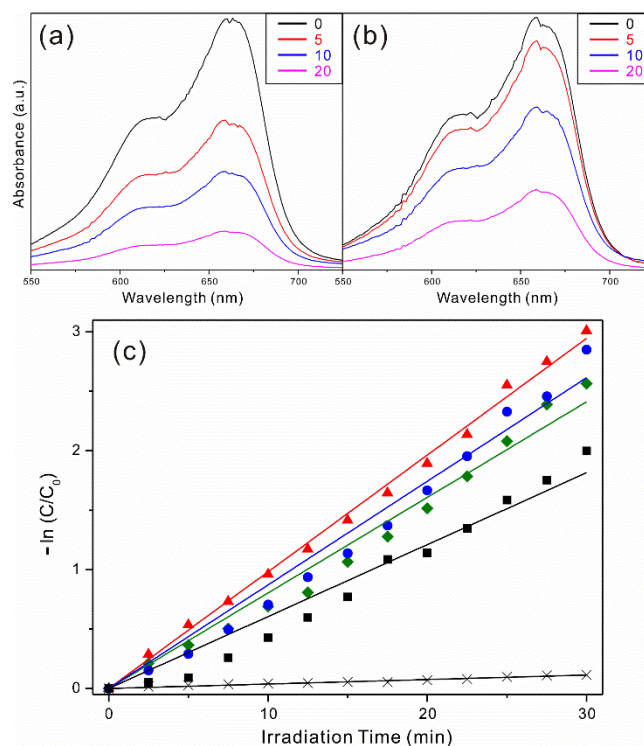


**Figure 2-6.** Photocatalytic absorption spectral changes of methylene blue(aq) in the presence of TiO<sub>2</sub> nanoblossoms grown at (a)  $f_w = 0.5$  and (b)  $f_w = 1$  with elapsed times indicated in the units of min. (c) First-order kinetic plots for the photocatalytic degradation of methylene blue in the presence of TiO<sub>2</sub> nanoblossoms grown at  $f_w$  values of (diamonds) 0.4, (triangles) 0.5, (circles) 0.6, and (squares) 1. The kinetic plot of crosses was obtained in the absence of TiO<sub>2</sub> nanoblossoms. The rate constants obtained from the best-fitted lines are given in Table 2-1.

first-order kinetic plots of Figure 2-6c demonstrate that TiO<sub>2</sub> nanoblossoms grown at  $f_w = 0.5$  have the most efficient photocatalytic activity. The photodegradation rate constant of methylene blue in the presence of TiO<sub>2</sub> nanoblossoms grown with  $f_w = 0.5$  is  $5.89 \text{ h}^{-1}$ , whereas that in the absence of any TiO<sub>2</sub> nanoblossoms is  $0.226 \text{ h}^{-1}$ , revealing that the actual photocatalytic rate constant of TiO<sub>2</sub> nanoblossoms grown with  $f_w = 0.5$  becomes  $5.66 \text{ h}^{-1}$ . The enhanced photocatalytic activity of TiO<sub>2</sub> nanoblossoms grown at  $f_w = 0.5$  has been attributed to their well-defined nanoscale p-n junctions arising from their excellent cocrystalline structures consisting of the anatase and the rutile tiny crystallites. Inner electric fields generated at the definite p-n junctions in TiO<sub>2</sub> nanoblossoms grown at  $f_w = 0.5$  have been considered to induce best photocatalytic performances.



## 2.5. Conclusions

We have facilely fabricated blossom-like TiO<sub>2</sub> nanoparticles via a solvothermal reaction of titanium foil in mixed solvents of water and EG. The morphological, structural, and optical properties of TiO<sub>2</sub> nanoblossoms have been controlled well by varying the relative amount of water in mixed solvents. Our TiO<sub>2</sub> nanoblossoms have cocrystalline structures having both the anatase and the rutile crystals; the proportion of the anatase structures in TiO<sub>2</sub> nanoblossoms has been increased as the volume fraction of water in mixed solvents ( $f_w$ ) increases. TiO<sub>2</sub> nanoblossoms having the highest photocatalytic performances have been fabricated at the optimum solvent condition that  $f_w$  is 0.5. In this condition, TiO<sub>2</sub> nanoblossoms have been found to have the anatase and rutile structures almost equivalently, indicating that well-defined nanoscale p-n junctions, which help to enhance catalytic performances via forming definite inner electric fields, have been formed between the anatase and the rutile domains. Also, TiO<sub>2</sub> nanoblossoms grown at  $f_w = 0.5$  have the smallest crystallite diameters, revealing that the tiny crystal domains of the two structures are dispersed well to form definite nanoscale p-n junctions. This is also supported by the abundant presence of oxygen vacancies in TiO<sub>2</sub> nanoblossoms grown with  $f_w = 0.5$ . Thus, TiO<sub>2</sub> nanoblossoms grown at  $f_w = 0.5$  show the best photocatalytic activity, which is mainly attributed to the best-defined nanoscale p-n junctions resulting from their excellent cocrystalline structures.

## **2.6. Acknowledgment**

This work was supported by the National Research Foundation of Korea (NRF) grant funded by the Korea government (MSIP) (No. 2011-0028981 and 2012-006345). D.J.J. is also thankful to the SRC program of NRF (2007-0056095).

## 2.7. Supporting Information

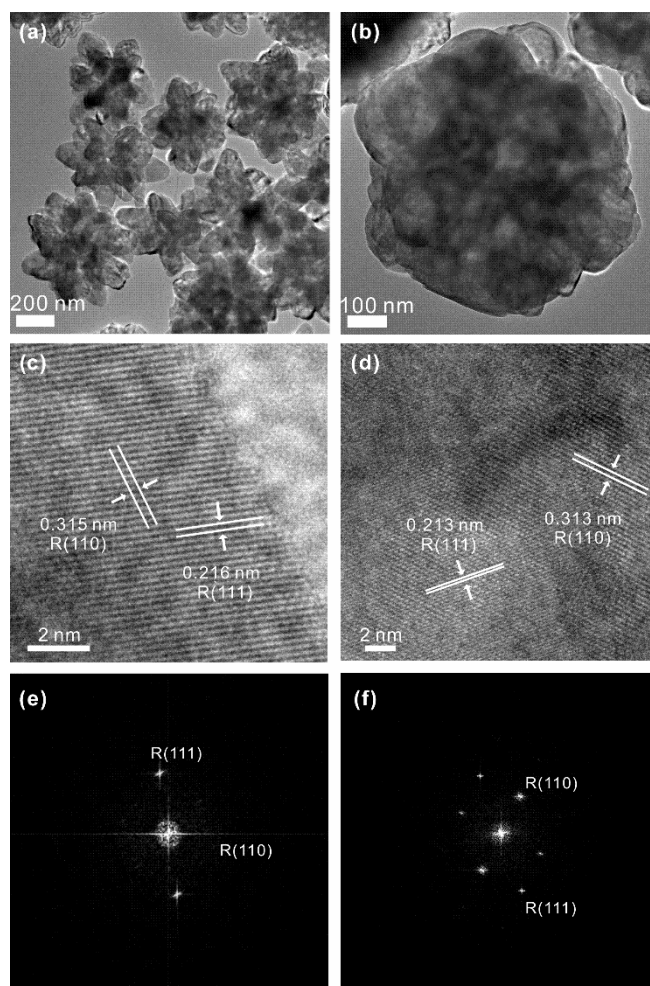


**Figure 2-S1.** (a,b) TEM images, (c,d) HRTEM images, and (e,f) FFT patterns of  $\text{TiO}_2$  nanoblossoms grown on Ti foil in mixture solvents of water and EG with  $f_w$  values of (a,c,e) 0.4 and (b,d,f) 0.6.

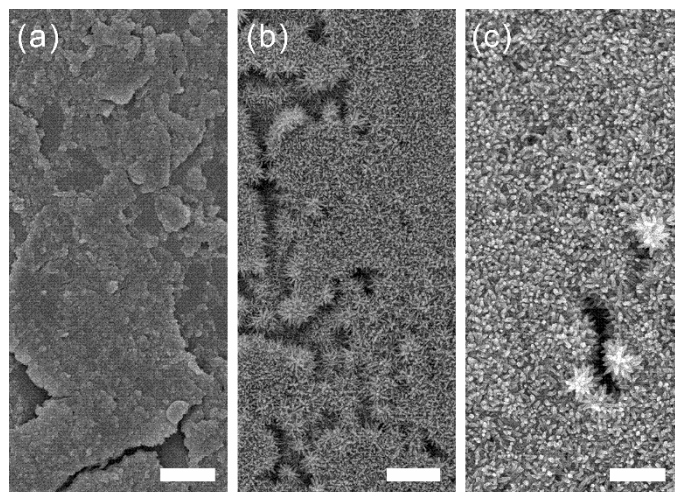


**Figure 2-S2.** FESEM images of TiO<sub>2</sub> nanostructures grown on Ti foil in mixture solvents of water and EG with  $f_w$  values of (a) 0, (b) 0.1, and (c) 0.25. Each scale bar indicates 1  $\mu\text{m}$ .

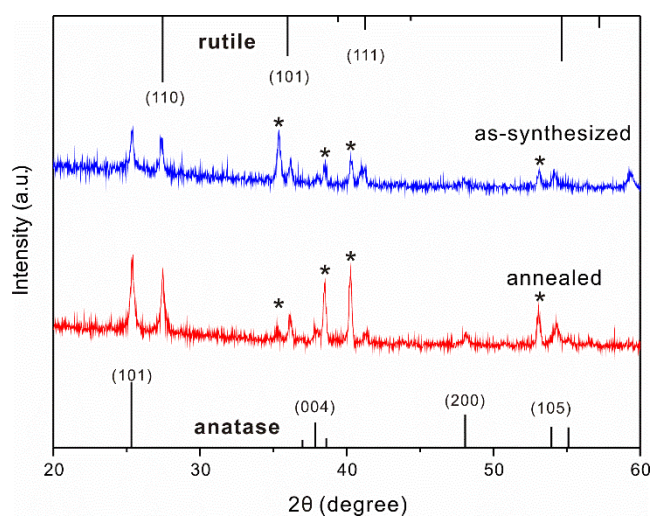


**Figure 2-S3.** HRXRD patterns of as-synthesized and annealed TiO<sub>2</sub> nanoblossoms grown on Ti foil in mixture solvents of water and EG with  $f_w = 0.5$ . The standard diffraction lines of anatase and rutile TiO<sub>2</sub> are also shown for comparison. The asterisks indicate diffraction peaks of bare Ti foil.

## 2.8. References

- [1] Kwak, J.-A.; Lee, D. K.; Jang, D.-J. *Appl. Catal. B: Environ.* **2013**, *142-143*, 323-328.
- [2] Son, M.; Kim, S. J.; Kim, J.-Y.; Jang, D.-J. *J. Nanosci. Nanotech.* **2013**, *13*, 5777-5782.
- [3] Skrabalak, S. E.; Au, L.; Li, X.; Xia, Y. *Nat. Protoc.* **2007**, *9*, 2182-2190.
- [4] Kim, M. R.; Kim, J.-Y.; Kim, S. J.; Jang, D.-J. *Appl. Catal. A-Gen.* **2011**, *393*, 317-322.
- [5] Zhang, Y.-Y.; Kim, J.-Y.; Kim, Y.; Jang, D.-J. *J. Nanopart. Res.* **2012**, *14*, 1117-1125.
- [6] Fujisjima, A.; Zhang, X. T.; Tryk, D. A. *Surf. Sci. Rep.* **2008**, *63*, 515-582.
- [7] Kim, J.-Y.; Jeong, H.; Jang, D.-J. *J. Nanopart. Res.* **2011**, *13*, 6699-6706.
- [8] Kim, H.-B.; Jang, D.-J. *CrystEngComm* **2012**, *14*, 6946-6951.
- [9] Kim, Y.; Kim, J.-Y.; Jang, D.-J. *J. Phys. Chem. C* **2012**, *116*, 10296-10302.
- [10] Kim, E. Y.; Park, J. H.; Han, G. Y. *J. Power Sources* **2008**, *184*, 284-287.
- [11] Joo, S.; Muto, I.; Hara, N. *J. Electrochem. Soc.* **2010**, *157*, J221-J226.
- [12] Rawal, S. B.; Bera, S.; Lee, D.; Jang, D.-J.; Lee, W. I. *Catal. Sci. Technol.* **2013**, *3*, 1822-1830.
- [13] Xu, C.; Shin, P. H.; Cao, L.; Wu, J.; Gao, D. *Chem. Mater.* **2010**, *22*, 143-148.
- [14] Varghese, O. K.; Paulose, M.; LaTempa, T. J.; Grimes, C. A. *Nano Lett.* **2010**, *10*, 750-750.
- [15] V. Leitner, N. K.; Doré, M. *Water Res.* **1997**, *31*, 1383-1397.
- [16] Schuchmann, M. N.; Zegota, H.; Vonsonntag, C. Z. *Naturforsch. B* **1985**, *40*, 215-221.
- [17] Benson, S. W. *J. Am. Chem. Soc.* **1965**, *87*, 972-979.
- [18] Russell, G. A. *J. Am. Chem. Soc.* **1957**, *79*, 3871-3877.
- [19] Tan, Y.; Lim, Y. B.; Altieri, K. E.; Seitzinger, S. P.; Turpin, B. J. *Atmos. Chem. Phys.* **2012**, *12*,

801-813.

[20] Hou, J.; Yang, X.; Lv, X.; Huang, M.; Wang, Q.; Wang, J. *J. Alloys Compd.* **2012**, *511*, 202-208.

[21] Allam, N. K.; Grimes, C. A. *Langmuir* **2009**, *25*, 7234-7240.

[22] Periyat, P.; Leyland, N.; McCormack, D. E.; Colreavy, J.; Corr, D.; Pillai, S. C. *J. Mater. Chem.* **2010**, *20*, 3650-3655.

[23] Bosc, F.; Ayrat, A.; Albouy, P.-A.; Guizard, C. *Chem. Mater.* **2003**, *15*, 2463-2468.

[24] Kim, J.-Y.; Lee, D.; Kim, H. J.; Lim, I.; Lee, W. I.; Jang, D.-J. *J. Mater. Chem. A* **2013**, *1*, 5982-5988.

[25] Liu, M.; Piao, L.; Zhao, L.; Ju, S.; Yan, Z.; He, T.; Zhou, C.; Wang, W. *Chem. Commun.* **2010**, *46*, 1664-1666.

[26] Liu, M.; Piao, L.; Lu, W.; Ju, S.; Zhao, L.; Zhou, C.; Li, H.; Wang, W. *Nanoscale* **2010**, *2*, 1115-1117.

[27] Yang, X. H.; Li, Z.; Sun, C.; Yang, H. G.; Li, C. *Chem. Mater.* **2011**, *23*, 3486-3494.

[28] Liu, X.; Hu, R.; Xiong, S.; Liu, Y.; Chai, L.; Bao, K.; Qian, Y. *Mater. Chem. Phys.* **2009**, *114*, 213-216.

[29] Wang, D.; Yu, R.; Kumada, N.; Kinomura, N. *Chem. Mater.* **1999**, *11*, 2008-2012.

[30] Yang, J.; Li, C.; Quan, Z.; Zhang, C.; Yang, P.; Li, Y.; Yu, C.; Lin, J. *J. Phys. Chem. C*, 2008, **112**, 12777-12785.

[31] Sridharan, K.; Park, T. J. *Appl. Catal. B-Environ.* **2013**, *134-135*, 174-184.

[32] Chen, X.; Wang, X.; Wang, Z.; Wan, J.; Liu, J.; Qian, Y. *Nanotechnology*, **2004**, *15*, 1685.

[33] Jia, Z.; Ren, D.; Wang, Q.; Zhu, R. *Appl. Surf. Sci.* **2013**, *270*, 312-318.

- [34] Jiang, X.; Wang, Y.; Herricks, T.; Xia, Y. *J. Mater. Chem.* **2004**, *14*, 695-703.
- [35] Shimizu, K.; Imai, H.; Hirashima, H.; Tsukuma, K. *Thin Solid Films* **1999**, *351*, 220-224.
- [36] Tian, B.; Chen, F.; Zhang, J.; Anpo, M. *J. Colloid. Interf. Sci.* **2006**, *303*, 142-148
- [37] Lan, C.-M.; Liu, S.-E.; Shiu, J.-W.; Hu, J.-Y.; Lin, M.-H.; Diao, E. W.-G. *RSC Adv.* **2013**, *3*, 559-565
- [38] Muhlebach, J.; Muller, K.; Schwarzenbach, G. *Inorg. Chem.* **1970**, *9*, 2381-2390.
- [39] Ichinose, H.; Terasaki, M.; Katsuki, H. *J. Sol-Gel Sci. Technol.* **2001**, *22*, 33-40.
- [40] Zhang, J.; Tang, X.; Li, D. *J. Phys. Chem. C* **2011**, *115*, 21529-21534.
- [41] Yoriya, S.; Mor, G. K.; Sharma, S.; Grimes, C. A. *J. Mater. Chem.* **2008**, *18*, 3332-3336.
- [42] Varghese, O. K.; Gong, D.; Paulose, M.; Grimes, C. A.; Dickey, E. C. *J. Mater. Res.* **2003**, *18*, 156-165.
- [43] Yang, Y.; Wang, X.; Li, L. *J. Am. Ceram. Soc.* **2008**, *91*, 632-635.
- [44] Lin, X.; Xing, J.; Wang, W.; Shan, Z.; Xu, F.; Huang, F. *J. Phys. Chem. C* **2007**, *111*, 18288-18293.
- [45] Weller, H. *Angew. Chem., Int. Ed.* **1993**, *32*, 41-53.
- [46] Savage, N.; Chwierothe, B.; Ginwalla, A.; Patton, B. R.; Akbar, S. A.; Dutta, P. K. *Sens. Actuators B* **2001**, *79*, 17-27.
- [47] Kim, J.-Y.; Kim, M. R.; Park, S.-Y.; Jang, D.-J. *CrystEngComm* **2010**, *12*, 1803-1808.
- [48] Bandaranayake, R. J.; Wen, G. W.; Lin, L. Y.; Jiang, H. X.; Sorensen, C. M. *Appl. Phys. Lett.* **1995**, *67*, 831-833.
- [49] Kim, Y.; Jang, D.-J. *Chem. Commun.* **2013**, *49*, 8940-8942.
- [50] Lei, Y.; Zhang, L. D.; Meng, G. W.; Li, G. H.; Zhang, X. Y.; Liang, C. H.; Chen, W.; Wang, S.

X. *Appl. Phys. Lett.* **2001**, 78, 1125-1127.

[51] Wu, J.-J.; Yu, C.-C. *J. Phys. Chem. B* **2004**, 108, 3377-3379.

[52] Koffyberg, F. P.; Dwight, K.; Wold, A. *Solid State Commun.* **1979**, 30, 433-437.

[53] Rahman, M.M.; Krishna, K.M.; Soga, T.; Jimbo, T.; Umeno, M. *J. Phys. Chem. Solids* **1999**, 60, 201-210.

[54] Li, J.-G.; Ishigaki, T.; Sun, X. *J. Phys. Chem. C* **2007**, 111, 4969-4976

[55] Kim, J.; Choi, W.; Park, H. *Res. Chem. Intermed.* **2010**, 36, 127-140.

[56] Nguyen-Phan, T.-D.; Shin, E. W. *J. Ind. Eng. Chem.* **2011**, 17, 397-400.

[57] Xiao, F. X. *J. Mater. Chem.* **2012**, 22, 7819-7830.

[58] Wilhelm, P.; Stephan, D. *J. Photochem. Photobiol. A* **2007**, 185, 19-25.



## Appendices

### A.1. List of Presentations

#### A.1.1. International Presentation

1. **Daeki Lee**, Wan-In Lee and Du-Jeon Jang, “Thermal Annealing-Free Room-Temperature Fabrication of Crystalline TiO<sub>2</sub> Nanotube Arrays”, *The first Photocatalysis and Solar Energy Convention: Development of Materials and Nanomaterials*, Daejeon, Korea (2012).
2. Jong-Yeob Kim, **Daeki Lee**, and Du-Jeon Jang, “Well-Ordered ZnO Nanowire Arrays for Ultraviolet Nanolasers”, *International Symposium on Small Particles and Inorganic Clusters XVI*, Leuven, Belgium (2012).

#### A.1.2. Domestic Presentation

1. **Daeki Lee**, Wan-In Lee and Du-Jeon Jang, “One-Step Fabrication of Anatase TiO<sub>2</sub> Nanotube Arrays at Room Temperature”, *The 109<sup>th</sup> Spring Meeting of the Korean Chemical Society*, Goyang, Korea (2012).
2. **Daeki Lee**, Wan-In Lee and Du-Jeon Jang, “Fabrication of Anodic TiO<sub>2</sub> Nanotube Arrays Coated with Crystalline TiO<sub>2</sub> Particles at Room Temperature”, *The 110<sup>th</sup> Autumn Meeting of the Korean Chemical Society*, Busan, Korea (2012).

## Abstract (Korean)

티타늄 포일을 기반으로 한 결정성 이산화티타늄 나노구조체를 양극화 반응과 용매열 합성법을 이용하여 쉽게 합성하였으며 이들의 형태구조적, 결정구조적, 광학적 특성들을 평가, 연구 하였다. 또한 합성된 결정성 이산화티타늄 나노구조체를 이용하여 광촉매 및 광전지 등 광전적 응용분야에 대한 연구를 실시하였다.

1장에서는 균일한 다공성을 가진 잘 배열된 아나타제 이산화티타늄 나노튜브 집합체를 티타늄 포일을 이용한 양극화 반응을 통해 에틸렌 글리콜과 글리세롤을 혼합한 점성용매 내에서 합성한 연구를 기술하였다. 혼합된 두 용매의 비율을 조절함으로써 이산화티타늄 나노튜브 집합체의 형태적, 결정적 구조를 제어하였다. 합성된 이산화티타늄 나노튜브 집합체는 혼합용매의 점성도에 따라 향상된 (004)면을 가짐으로 인해 더욱 활성화 된 촉매반응을 보일 수 있었다. 전체 합성된 이산화티타늄 나노튜브 집합체 중 에틸렌 글리콜과 글리세롤이 2:1의 비율로 혼합된 용매 내에서 생성된 이산화티타늄 나노튜브 집합체가 가장 높은 광촉매적 특성을 보였으며 또한 4.08% 효율의 가장 높은 광전지적 특성을 함께 보임을 확인하였다.

2장에서는 추가적인 어닐링 과정 없이 아나타제와 루타일의 공결정성을 가지는 나노꽃 구조의 이산화티타늄을 티타늄 포일을 이용한 용매열 합성법을 통하여 물과 에틸렌 글리콜을 혼합한 용매 내에서 합성한 연구를 기술하였다. 혼합용매 내 물과 에틸렌 글리콜의 비율을 조절하여 나노꽃 구조 이산화티타늄의 형태구조적, 결정구조적, 광학적 특성을 쉽게 제어하였다. 용매 내 에틸렌

글리콜의 영향으로 인해 생성된 나노꽃 구조 이산화티타늄의 공결정성 구조는 재료 내에서 나노규모의 p-n 접합구조 역할을 하여 내부 전기장을 생성하고 이를 통해 촉매활성을 더욱 증가시키는데 도움 줌을 확인하였다. 특히 1:1의 비율로 물과 에틸렌 글리콜이 혼합된 용매 내에서 생성된 나노꽃 구조 이산화티타늄이 가장 좋은 공결정 구조를 가짐으로써 최고의 광촉매적 특성을 가짐을 확인하였다.

주요어: 이산화티타늄, 양극화 반응, 나노튜브 접합체, 점성용매, 용매열 합성, 나노꽃 구조, 나노규모 p-n 접합구조, 광전적 반응

학번: 2011-23234